

Paleoceanography and Paleoclimatology

RESEARCH ARTICLE

10.1029/2020PA003994

Key Points:

- Extended composite and correlated equivalent depth scales are presented for Antarctic proximal International Ocean Discovery Program Sites U1536 and U1537
- U1536 and U1537 have excellent magnetostratigraphy and clear imprint of orbital variations in their lithology
- Changes in terrigenous versus diatomaceous Dove Basin facies are out of phase with benthic $\delta^{18}\text{O}$ during intervals between 3.3 and 1 Ma

Supporting Information:

- Supporting Information S1
- Table S1

Correspondence to:

B. T. Reilly,
breilly@ucsd.edu

Citation:

Reilly, B. T., Tauxe, L., Brachfeld, S., Raymo, M., Bailey, I., Hemming, S., et al. (2021). New magnetostratigraphic insights from iceberg alley on the rhythms of Antarctic climate during the Plio-Pleistocene. *Paleoceanography and Paleoclimatology*, 36, e2020PA003994. <https://doi.org/10.1029/2020PA003994>

Received 28 MAY 2020

Accepted 11 JAN 2021

New Magnetostratigraphic Insights From Iceberg Alley on the Rhythms of Antarctic Climate During the Plio-Pleistocene

Brendan T. Reilly¹ , Lisa Tauxe¹ , Stefanie Brachfeld² , Maureen Raymo³ , Ian Bailey⁴ , Sidney Hemming³ , Michael E. Weber⁵ , Trevor Williams⁶, Marga Garcia⁷ , Michelle Guitard⁸, Yasmina M. Martos^{9,10} , Lara F. Pérez¹¹ , Xufeng Zheng¹² , Linda Armbrecht¹³, Fabricio G. Cardillo¹⁴, Zhiheng Du¹⁵, Gerson Fauth¹⁶ , Anna Glueder¹⁷, Marcus Gutjahr¹⁸ , Iván Hernández-Almeida¹⁹ , Frida S. Hoem²⁰ , Ji-Hwan Hwang²¹, Mutsumi Iizuka²², Yuji Kato²³ , Bridget Kenlee²⁴ , Suzanne O'Connell²⁵ , Victoria Peck¹¹, Thomas A. Ronge²⁶ , Osamu Seki²⁷ , Shubham Tripathi²⁸ , and Jonathan Warnock²⁹ 

¹Scripps Institution of Oceanography, University of California San Diego, La Jolla, CA, USA, ²Earth and Environmental Studies, Montclair State University, Montclair, NJ, USA, ³Lamont-Doherty Earth Observatory, Columbia University, Palisades, NY, USA, ⁴Camborne School of Mines and Environmental Sustainability Institute, University of Exeter, Penryn Campus, Cornwall, UK, ⁵Institute for Geosciences, University of Bonn, Bonn, Germany, ⁶International Ocean Discovery Program, Texas AM University, College Station, TX, USA, ⁷Oceanographic Center of Cadiz, Spanish Institute of Oceanography (IEO), Cádiz, Spain, ⁸College of Marine Science, University of South Florida, St. Petersburg, FL, USA, ⁹Planetary Magnetospheres Laboratory, NASA Goddard Space Flight Center, Greenbelt, MD, USA, ¹⁰Department of Astronomy, University of Maryland College Park, College Park, MD, USA, ¹¹British Antarctic Survey, Cambridge, UK, ¹²South China Sea Institute of Oceanology, Chinese Academy of Sciences, Guangzhou, China, ¹³Australian Centre for Ancient DNA, Department of Ecology & Evolutionary Biology, University of Adelaide, Adelaide, SA, Australia, ¹⁴Departamento Oceanografía, Servicio de Hidrografía Naval, Argentina, ¹⁵State Key Laboratory of Cryospheric Science, Northwest Institute of Eco-Environment and Resources, Chinese Academy of Sciences, Lanzhou, China, ¹⁶Geology Program, University of Vale do Rio dos Sinos, São Leopoldo, RS, Brazil, ¹⁷College of Earth, Ocean, and Atmospheric Sciences, Oregon State University, Corvallis, OR, USA, ¹⁸GEOMAR Helmholtz Centre for Ocean Research Kiel, Kiel, Germany, ¹⁹Department of Earth Sciences, ETH Zürich, Zurich, Switzerland, ²⁰Department of Earth Sciences, Marine Palynology and Paleoceanography, Utrecht University, Utrecht, The Netherlands, ²¹Earth Environmental Sciences, Korea Basic Science Institute, Cheongju, Republic of Korea, ²²Knowledge Engineering, Tokyo City University, Setagaya-ku, Tokyo, Japan, ²³Center for Advanced Marine Core Research, Kochi University, Nankoku, Kochi, Japan, ²⁴Department of Earth Sciences, University of California Riverside, Riverside, CA, USA, ²⁵Department of Earth and Environmental Sciences, Wesleyan University, Middletown, CT, USA, ²⁶Helmholtz Center for Polar and Marine Research, Alfred Wegener Institute, Bremerhaven, Germany, ²⁷Institute of Low Temperature Science, Hokkaido University, Sapporo, Hokkaido, Japan, ²⁸Marine Stable Isotope Lab, National Centre for Polar and Ocean Research, Ministry of Earth Sciences, Vasco Da Gama, India, ²⁹Department of Geoscience, Indiana University of Pennsylvania, Indiana, PA, USA

Abstract International Ocean Discovery Program (IODP) Expedition 382 in the Scotia Sea's *Iceberg Alley* recovered among the most continuous and highest resolution stratigraphic records in the Southern Ocean near Antarctica spanning the last 3.3 Myr. Sites drilled in Dove Basin (U1536/U1537) have well-resolved magnetostratigraphy and a strong imprint of orbital forcing in their lithostratigraphy. All magnetic reversals of the last 3.3 Myr are identified, providing a robust age model independent of orbital tuning. During the Pleistocene, alternation of terrigenous versus diatomaceous facies shows power in the eccentricity and obliquity frequencies comparable to the amplitude modulation of benthic $\delta^{18}\text{O}$ records. This suggests that variations in Dove Basin lithostratigraphy during the Pleistocene reflect a similar history as globally integrated ice volume at these frequencies. However, power in the precession frequencies over the entire ~3.3 Myr record does not match the amplitude modulation of benthic $\delta^{18}\text{O}$ records, suggesting Dove Basin contains a unique record at these frequencies. Comparing the position of magnetic reversals relative to local facies changes in Dove Basin and the same magnetic reversals relative to benthic $\delta^{18}\text{O}$ at North Atlantic IODP Site U1308, we demonstrate Dove Basin facies change at different times than benthic $\delta^{18}\text{O}$ during intervals between ~3 and 1 Ma. These differences are consistent with precession phase shifts and suggest climate signals with a Southern Hemisphere summer insolation phase were recorded around Antarctica. If Dove Basin lithology reflects local Antarctic ice volume changes,

these signals could represent ice sheet precession-paced variations not captured in benthic $\delta^{18}\text{O}$ during the 41-kyr world.

1. Introduction

Earth's climate state has undergone several significant changes during the last 3.3 Myr, including the initiation of expanded bipolar glaciation around Plio-Pleistocene boundary time (Bailey et al., 2013; Jansen et al., 2000; Shackleton et al., 1984) and changes in the amplitude and frequency of glacial-interglacial variations during the mid-Pleistocene transition (MPT; Clark et al., 2006; Pisias & Moore, 1981; Ruddiman et al., 1989). While it has long been accepted that the pacing of Plio-Pleistocene glacial-interglacial cycles is driven by changes in the eccentricity (~ 100 kyr), obliquity (41 kyr), and precession (19–23 kyr) of Earth's orbit (Hays et al., 1976), our understanding of the drivers of long-term changes and transitions is incomplete.

Benthic $\delta^{18}\text{O}$ is a key parameter in paleoceanography for understanding global climate evolution and is often used to study Plio-Pleistocene ice sheet response to orbital forcing through the amplitude evolution of its orbital frequencies (e.g., Liautaud et al., 2020; Lisiecki & Raymo, 2007) and as a constraint for ice sheet evolution models (de Boer et al., 2014; Pollard & DeConto, 2009). Three main features of Plio-Pleistocene benthic $\delta^{18}\text{O}$ records are as follows: (1) obliquity frequency amplitude modulation ($1/41$ kyr $^{-1}$) that matches the amplitude modulation of the orbital forcing prior to 1.4 Ma, (2) amplitude evolution of the precession frequencies ($1/19$ – $1/23$ kyr $^{-1}$) that is similar to the amplitude modulation of the orbital forcing but increases exponentially during the Pleistocene, and (3) an increase in $\sim 1/100$ kyr $^{-1}$ eccentricity frequency amplitude after 1.4 Ma that does not match orbital forcing (Lisiecki & Raymo, 2007). However, on orbital and longer timescales, benthic $\delta^{18}\text{O}$ is a complicated proxy for ice sheet histories as it is a combined signal of global ice volume and deep sea temperature (Shackleton, 1967). Deconvolving that signal requires records of deep sea temperature (e.g., Elderfield et al., 2012; Ford et al., 2016; Sosdian & Rosenthal, 2009), sea level changes (e.g., Grant et al., 2019; Rohling et al., 2014), and stratigraphic records with signals directly influenced by Northern and Southern Hemisphere ice sheets (e.g., Naish et al., 2009; Patterson et al., 2014; Shakun et al., 2016).

A long-standing debate surrounds the origin of the strong 41 kyr cyclicity and nearly absent 19–23 kyr precession cyclicity observed in records of benthic $\delta^{18}\text{O}$ during the late Pliocene and early Pleistocene (~ 3.1 Ma; Raymo & Huybers, 2008; Raymo & Nisancioglu, 2003; Raymo et al., 1989; Ruddiman et al., 1989; 1986). Many hypotheses have been offered, such as the role of integrated summer insolation (Huybers, 2006), the latitudinal gradient in insolation and resulting changes in moisture transport (Raymo & Nisancioglu, 2003), and cancellation of precession signals by out-of-phase Northern and Southern Hemisphere ice sheets responding to the intensity of summer insolation—the *Antiphase Hypothesis* (Raymo et al., 2006). Some data exist that suggest out-of-phase hemispheric precession signals were a feature of the 41 kyr world, including a precession signal with Southern Hemisphere phase in the Southern Ocean during Marine Isotope Stage (MIS) 31 around the lower C1r.1n (Jaramillo) magnetic reversal (~ 1.07 Ma; Scherer et al., 2008) and precession signals with a Northern Hemisphere phase in meltwater runoff from the North American Mississippi River drainage between 2.55 and 1.70 Ma (Shakun et al., 2016). In the framework of the Antiphase Hypothesis, the exponential increase of benthic $\delta^{18}\text{O}$ precession frequency amplitude (Lisiecki & Raymo, 2007) would not necessarily reflect a significant change in the sensitivity of ice sheets to precession forcing. Rather the small precession signal in the early Pleistocene would be the result of a ratio of Northern and Southern Hemisphere ice volume changes at precession frequencies near unity leading to destructive interference of each hemisphere's precession signal in the global signal (Moree et al., 2021; Raymo et al., 2006). More data are needed from ice sheet proximal environments to develop our understanding of the behavior of marine and terrestrial ice sheets during the 41 kyr world. New drill cores recovered during International Ocean Discovery Program (IODP) Expedition 382 “Iceberg Alley and Subantarctic Ice and Ocean Dynamics” offer one such opportunity since it recovered near-continuous and expanded late Pliocene to Holocene stratigraphic sections from Dove Basin in the Scotia Sea with lithostratigraphies that are from a region directly influenced by Antarctica's glacial history and Southern Ocean dynamics (e.g., Sprenk et al., 2013; Weber et al., 2014, 2012, 2019).

As benthic calcite-based $\delta^{18}\text{O}$ records cannot be generated from most Antarctic proximal marine sequences, the relationships between changes in Antarctic proximal sediment lithology, benthic $\delta^{18}\text{O}$, and orbital

curves are largely unknown for the Plio-Pleistocene. Assumptions must therefore be made about the orbital pacing of Antarctic climate when tuning a climate-sensitive parameter from such records to orbital curves or benthic $\delta^{18}\text{O}$. Accordingly, these assumptions limit our ability to test questions regarding the orbital forcing of Antarctic climate itself. By contrast, magnetostratigraphy, which uses geomagnetic variability driven by convection in the Earth's liquid outer core as a stratigraphic tool, is independent of climate and has been central to the establishment of the timing and pacing of paleoclimatic signals since its earliest applications (Hays et al., 1976; Huybers, 2007; Imbrie et al., 1984; Opdyke et al., 1966; Raymo et al., 1989; Ruddiman et al., 1989; Shackleton & Opdyke, 1973, and many others). Discontinuous magnetostratigraphically and biostratigraphically calibrated Antarctic proximal sediments have provided valuable insights into the history of the Antarctic Ice Sheet, with those deposited in the Ross Sea interpreted as showing that ~41-kyr timescale changes in Antarctic Ice Sheet extent were likely important during the Pliocene (e.g., Naish et al., 2009). However, the discontinuous nature of such records limits our ability to assess the phase and the relative strength of the various orbital frequencies pacing Antarctic Ice Sheet extent in the late Pliocene and early Pleistocene, such as the suggestion that Antarctica experienced precession and eccentricity-paced variations in the late Pliocene from a magnetostratigraphically calibrated ice-rafted debris (IRD) record from the Wilkes Land Margin (Patterson et al., 2014). Here, we present an exceptional, continuous, and high-resolution late Pliocene to Holocene geomagnetic polarity stratigraphy from IODP Expedition 382 Sites U1536 and U1537 and use it to examine the Antarctic Ice Sheet and Southern Hemisphere climate response to orbital forcing relative to benthic $\delta^{18}\text{O}$ during the 41 kyr world.

2. Materials and Methods

2.1. Dove Basin

Dove Basin is one of several oceanic basins in the southern Scotia Sea with thick contourite deposits formed by the influence of the eastward flowing Antarctic Circumpolar Current, the northward flowing Weddell Sea Deep Water, and, on long timescales, by regional tectonics (e.g., Maldonado et al., 2003; Pérez et al., 2017) (Figure 1). The Scotia Sea constitutes a back-arc system where the active spreading center at the East Scotia Ridge leads to regional compression along the southern Scotia Sea basins (Pérez et al., 2017). Large-scale variability in contourite deposition in the Scotia Sea is related to long-term changes in bottom water flows. These oceanographic changes have been influenced by ice sheet and tectonic events, with the latter including uplift of the Shackleton Fracture Zone around the time that Dove Basin's seismic reflector-c was formed (8.4–14.2 Ma; Pérez et al., 2021). Uplift of the Shackleton Fracture Zone potentially continued to occur through when Dove Basin's seismic reflector-a formed (1.4–1.8 Ma; Pérez et al., 2021). While modeling work suggests changes in dynamic topography over the last 3 Ma were significant for sectors of East Antarctica, changes were less significant for the Weddell Sea sector of Antarctica and the Antarctic Peninsula (Austermann et al., 2015).

Lateral transport and sediment focusing in the Dove Basin contourite deposit allowed for high sedimentation rates in the late Quaternary, ranging from ~20 to 100 cm/kyr (as evidenced from Calypso Core MD07-3134; Sprenk et al., 2013; Weber et al., 2012), and thick stratigraphic sequences in excess of 1 km that are hypothesized to extend from the present to the early Miocene (Pérez et al., 2017). Late Quaternary focusing factors, the ratio of total sediment flux to the vertical settling sediment flux, calculated from excess ^{230}Th in Core MD07-3134, are variable on orbital timescales and range from 5 to 13 during interglacial intervals and 11 to 29 during glacial intervals (Sprenk et al., 2013).

Dove Basin also lies beneath an export pathway for Antarctic icebergs, named *Iceberg Alley* (Anderson & Andrews, 1999). Icebergs are calved from all sectors of Antarctica and predominantly travel counterclockwise around the continent in the Antarctic Coastal Current until they reach the Weddell Sea Gyre. Here, they travel north and, ultimately, reach the warmer Antarctic Circumpolar Current where they melt and shed their terrigenous load (Budge & Long, 2018). While icebergs transported through Iceberg Alley today are biased toward those sourced from the Weddell Sea sector of Antarctica (Budge & Long, 2018), the Dove Basin sediment record has the potential to contain IRD from far-traveled icebergs, effectively integrating signals of ice sheet mass loss from the entire Antarctic Ice Sheet. The high Dove Basin sedimentation rates and associated IRD records have previously allowed reconstructions of late Quaternary centennial to millennial scale variations in iceberg flux across this region (Bakker et al., 2016; Weber et al., 2014).

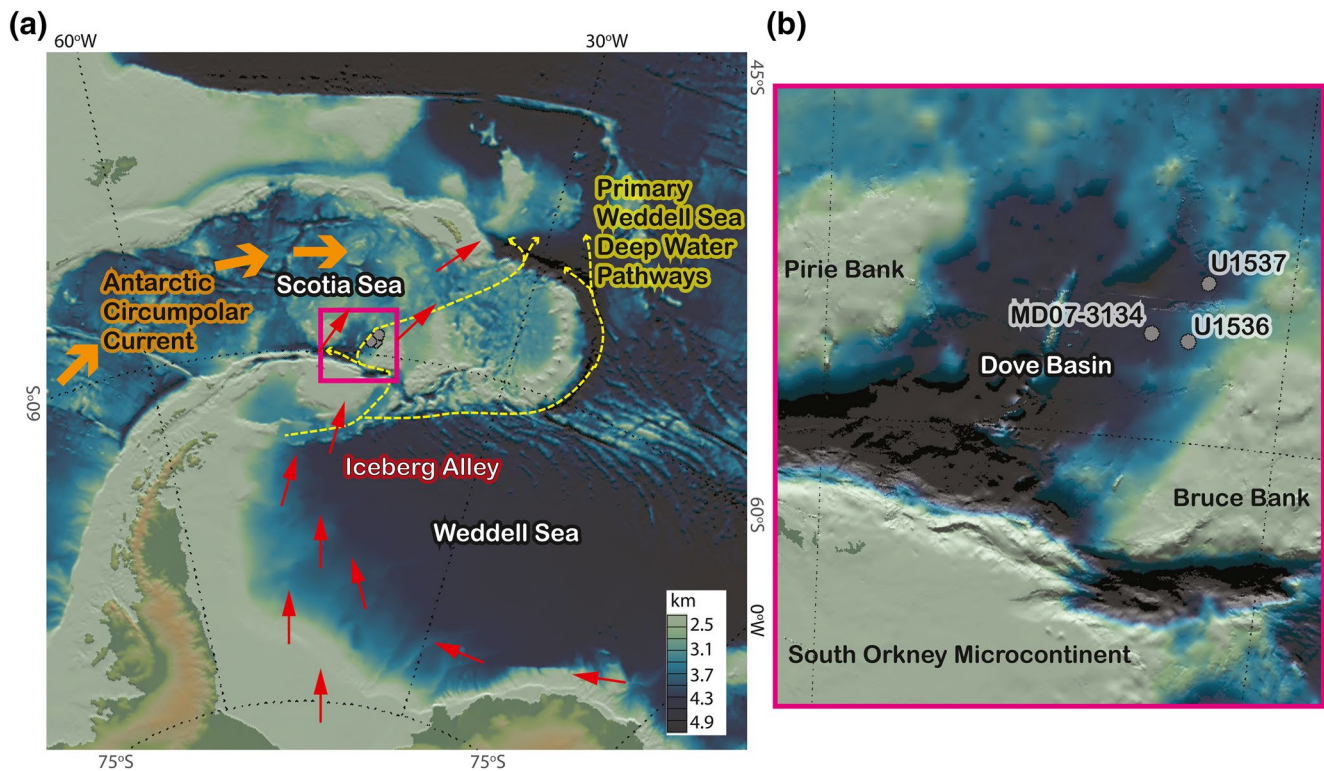


Figure 1. (a) Map of study area (b) with zoom in of Dove Basin, including Dove Basin core locations from IODP Expedition 382, U1536 and U1537 (Weber et al., 2019), and core MD07-3134 (Weber et al., 2012). In (a), red arrows indicate general iceberg export path through Iceberg Alley (Anderson & Andrews, 1999; Budge & Long, 2018), yellow dashed lines indicate primary pathways for Weddell Sea Deep Water (after Meredith et al., 2008), and orange arrows indicate the flow direction of the Antarctic Circumpolar Current. Base map is created using GeoMapApp (<http://www.geomapp.org>) and the Global Multi-Resolution Topography (GMRT) synthesis (Ryan et al., 2009). IODP, International Ocean Discovery Program.

Pliocene to Holocene sediment lithology in Dove Basin primarily alternates between diatom oozes and silty clays, with variable concentration of sand to gravel-sized clasts delivered as IRD (Weber et al., 2019). Detailed study of core MD07-3134 indicates that during the late Quaternary, diatom oozes were deposited during interglacial/warm times and silty clays were deposited during glacial/cold times (Sprenk et al., 2013; Weber et al., 2012). Longer records recovered during IODP Expedition 382 show continued alternation between diatom oozes and silty clays extending to at least 3.3 Ma. While variation in these two facies is not always evident visually, they are manifest in changes in the ratio of biogenic versus terrigenous concentration, which are clearly captured by shipboard continuous nondestructive measurements like spectral color, gamma ray attenuation (GRA)-derived wet bulk density (hereafter, simply GRA), and natural gamma radiation (NGR) (Sprenk et al., 2013; Weber et al., 2019).

2.2. IODP Expedition 382 Sites U1536 and U1537

IODP Expedition 382 drilled five sites from the Subantarctic Front drift off the southern tip of South America and the Dove and Pirie basins in the Scotia Sea, recovering sediments deposited from the middle Miocene to present (see Weber et al., 2019). We focus here on advanced piston core (APC) and half-length advanced piston core (HLAPC) intervals at Dove Basin Sites U1536 (~355 meters below seafloor [mbsf]) and U1537 (~330 mbsf), which recovered Pliocene- and Pleistocene-aged sediments (Weber et al., 2019) (Figure 1).

Five holes were drilled at Site U1536 with holes A, B, and C focused on deep APC/HLAPC coring (see Figure F7 in Weber et al., 2019). APC refusal started around 214 mbsf in hole A, and mixed APC and HLAPC cores recovered sediment to a depth of 290 mbsf in hole C. HLAPC cores were recovered to a maximum

depth of ~355 mbsf in hole A and ~352 mbsf in hole C. The focus of hole B was to provide overlap in key intervals and was a mix of drilled intervals and APC cores to a maximum depth of ~227 mbsf.

Four holes were drilled at Site U1537 with holes A and D focused on deep APC/HLAPC coring (see Figure F7 in Weber et al., 2019). APC refusal occurred around 240 mbsf in hole A and 244 mbsf in hole D. HLAPC extended hole A to a maximum depth of ~264 mbsf and hole D to a maximum depth of ~354 mbsf.

Recovery was generally excellent in APC/HLAPC cored intervals at Site U1536 and U1537, ranging from 90% to 103%. While core quality was often good, some cored intervals experienced variable levels of coring disturbance due to challenging weather conditions during high seas. The new *JOIDES Resolution* X-ray imaging system, first implemented during the preceding IODP Expedition 379 (Gohl et al., 2019), provided a means to monitor and account for coring disturbance from the interpretation of core data and construction of spliced composite records.

2.3. Shipboard Data

Paleomagnetic data collected on board the *JOIDES Resolution* during IODP Expedition 382 focused on investigating the sediment's natural remanent magnetization (NRM) and identifying the sediment's characteristic remanent magnetization (ChRM) direction that could be correlated to the polarity intervals of the geomagnetic polarity timescale. Data were collected from two primary sources—archive half sections and discrete Natsuhara-Giken (Japanese) cube samples (~7 cm³).

Remanence measurements were made using a 2G Enterprises Model 760R-4K superconducting rock magnetometer (SRM) equipped with direct-current superconducting quantum interference devices and an in-line, automated alternating field (AF) demagnetizer (Acton et al., 2017). NRM measurements of the archive half sections were made every 5 cm on the initial NRM and after AF demagnetization at 10 and 15 mT peak fields. At both sites, a 20 mT peak field was also initially used in the first hole but was discontinued after recognizing that the vertical drill string overprint (e.g., Richter et al., 2007) was removed by the 10 mT demagnetization step.

Vertically oriented discrete cube samples were collected from the working half sections at a sampling resolution of about one per section (~1.5 m) in hole A. Additional samples were taken from other holes when needed to fill in stratigraphic gaps (total samples: $n = 393$ for U1536; $n = 228$ for U1537). For all cubes, measurements were made of the initial NRM and following AF demagnetization at 0, 5, 10, and 15 mT peak AF. A subset of the cubes ($n = 23$ for U1536; $n = 12$ for U1537) were subjected to additional AF demagnetization up to 50 mT peak fields to further explore their NRM. For AF fields of 10 mT and higher, the cube samples were demagnetized and measured in three mutually perpendicular positions to monitor for and mitigate the influence of spurious anhysteretic remanent magnetizations (ARMs) and gyroremanent magnetizations (GRMs) (after Stephenson, 1993).

Continuous nondestructive physical properties of the sediments, such as spectral reflectance, NGR, and GRA, were collected during the expedition following standard IODP protocol (Blum, 1997) and used as tracers for lithologic variability (see Sprenk et al., 2013). NGR is proportional to the concentration of radioactive elements in the sediment, particularly K, U, and Th (De Vleeschouwer et al., 2017). In settings like Dove Basin, the first order control on NGR is the relative contribution of biogenic (diatom) sediments (NGR = 0 counts per second [cps]) versus lithogenic sediments (NGR ≥ 0 cps). Secondary controls could include lithogenic sediment particle size, as radioactive elements are often enriched in clays, and sediment provenance. GRA also captures this lithologic variability and shows a correlation with biogenic silica estimates in MD07-3134, with biogenic (diatom) sediments having lower wet bulk density than lithogenic sediments; however, GRA can also be influenced by lithogenic sediment particle size and sediment compaction (Sprenk et al., 2013; Weber et al., 2012, 1997). The spectral reflectance parameter, b^* , which tracks the blue-yellow color component of the sediment has also been shown to have a linear relationship with the biogenic silica contribution to sediments in Dove Basin during the late Quaternary (Sprenk et al., 2013).

Following late Quaternary observations, we interpret diatom oozes as having been deposited during warm times and silty clays as having been deposited during colder times (Sprenk et al., 2013; Weber

et al., 2012) but refer to these major lithologies using descriptive terminology as diatomaceous (low NGR, low GRA, high b^* diatom oozes) and terrigenous (high NGR, high GRA, low b^* silty clays) Dove Basin facies. Further work will still need to confirm whether the relationship between paleoenvironment and lithology in the late Pliocene and early Pleistocene is indeed consistent with the late Quaternary observations and how the trends in these records relate to long-term changes in temperature, oceanographic, and ice sheet evolution.

2.4. Correlated Equivalent Depth Scale

During IODP Expedition 382, composite spliced sedimentary sequences were generated for Site U1536 using intervals from holes A, B, and C to a depth of ~ 217 mbsf (~ 234 meters composite depth [mcd]) and for Site U1537 using intervals from holes A, B, and D to a depth of ~ 263 mbsf (~ 284 mcd). The length of each spliced record was determined by the depth to which correlations could confidently be made between holes (Tables S1 and S2). For this study, the U1536 and U1537 records were extended below the splice by appending recovered APC and HLAPC cores. This is a discontinuous record, as between ~ 10 and 150 cm of sediment is generally unrecovered between APC/HLAPC cored intervals even if overall recovery is greater than 100% (Ruddiman, Cameron et al., 1987). At the long-term sedimentation rates observed in Dove Basin (see Section 3.3), this could account for up to 30 kyr of missing time; however, some or all this missing time can be accounted for through stratigraphic comparison of U1536 and U1537.

For Site U1536, Cores U1536C-17F to U1536C-24F and Cores U1536A-40F to U1536A-53F were appended below the splice. A tie point between the two holes could be made with confidence at 285.4 mbsf in Core U1536C-24F and 288.14 mbsf in Core U1536A-40F (Table S1). For the appended sections, a growth factor of 7.5% was applied to all cores based on the observed growth factor of the cores near the base of the splice. Growth factors in the splice depth, calculated by the difference between the mbsf and mcd depth scales and often ranging from 5% to 20%, are typically attributed to postcoring expansion of the sediments (e.g., Hatfield et al., 2020; Lisiecki & Herbert, 2007). Following application of the growth factor, 3.2 m was subtracted from the depth of Cores U1536A-40F to U1536A-53F to align the tie point in Core U1536A-40F to Core U1536C-24F. These affine offsets, below the official splice, differ from those determined shipboard.

For U1537, Cores U1537D-33F to U1537D-45F were appended below the splice (Table S2). A growth factor of 7% was first applied to the cores based on the average growth factor calculated from the spliced interval. Then, 2.9 m was added to each of these cores to prevent overlap with the splice. Above these appends, the splice is the same as that determined during the expedition with one exception. Core U1537D-28F is used in this study instead of Core U1537A-28F, as coring deformation led to noticeably shallower inclinations in Core U1537A-28F while Core U1537D-28F inclinations are more like what would be expected based on the geocentric axial dipole hypothesis (i.e., $\tan I = 2 \tan \lambda$, where I is the expected inclination and λ is the site latitude; Hospers, 1954; McElhinny, 2007).

Despite differences in sedimentation rates and the ~ 20.5 m distance between drilling sites, lithologic variability tracked by NGR (high NGR = silty clay; low NGR = diatom ooze) shows remarkable similarity between the two sites (Weber et al., 2019). Accordingly, a correlated equivalent depth (ced) scale was generated for the U1536 spliced interval through correlation of the U1536 NGR pattern to U1537, excluding intervals identified as containing primarily slumped sediments in visual descriptions and/or X-ray images (Table S3). GRA, color reflectance, magnetic susceptibility, and paleomagnetic measurements were used as independent checks to guide the correlation. We quantify uncertainty associated with this correlation using Undatable MATLAB tools (Lougheed & Obrochta, 2019), by running 10,000 iterations of possible depth-depth correlations using an *xfactor* of 0.1, assuming ± 20 cm uncertainty in tie points in U1536 and U1537, and bootstrapping 25% of the tie points chosen below the U1536 splice. The latter constraint assumes that in each iteration, only 75% of the tie points used where cores are appended and recovery is incomplete are correct, providing a conservative uncertainty structure for the depth-depth relationship (Table S4). Data used in this study on these depth scales are available in Tables S5 and S6.

2.5. Data Stacks

Proxies for lithology that are regionally representative at individual sites can be complicated by local factors, such as incomplete recovery, slumps, IRD, or diagenesis. To extract signals representative of Dove Basin sedimentation, U1536 and U1537 data were stacked, removing intervals identified as being dominated by slumps (54.9–60.2 and 92.97–102.5 mcd in U1536; 209.5–215.7 mcd and below 304.9 mcd in U1537). NGR, GRA, and b^* stacks were generated following the method of Weber and Reilly (2018), by first interpolating to evenly spaced intervals using a Gaussian filter, with full width at half maximum for NGR based on the response function of the sensor (18 cm) and 10 cm for GRA and b^* (Walczak et al., 2015), and then averaging the two sites. For illustrative purposes, an inclination stack was generated by averaging archive half inclinations in binned intervals where both sites have data and keeping intervals where there is good agreement between the sites (differences of $<40^\circ$). We use the U1537 archive half inclination record for magnetostratigraphic interpretation, as it is primary data, can be interpreted with little ambiguity, and is in good agreement with the noisier U1536 archive half inclination record following NGR correlation. The data stacks are available in Table S13.

2.6. Age Models and Time Series Analysis

Age models were constrained by the sediment water interface (0 ka) and the magnetic reversals using Undatable MATLAB tools by running 10,000 iterations with a 0.1 *xfactor* (Lougheed & Obrochta, 2019). Uncertainty in the depth and age of the magnetic reversals, discussed below, are both considered in this method. Sedimentation rates are calculated in fixed 300 kyr increments, with uncertainty estimates calculated from the ensemble of Undatable age models. Fixed intervals, rather than the irregular spaced magnetic reversals, are used for sedimentation rate calculations to mitigate apparent sedimentation rate variability that could result from averaging time intervals of different lengths (e.g., Gulick et al., 2015; Mix, 2020).

The multitaper method (two tapers) was used for frequency analysis of the Dove Basin stacks, LR04 benthic $\delta^{18}\text{O}$ stack (Lisiecki & Raymo, 2005), and Laskar et al. (2004) climatic precision and obliquity angle orbital curves. Analysis was performed using the MATLAB implementation of Husson et al. (2014) every 50 kyr in 400-kyr wide intervals. To track the amount of power in frequency bands important for Plio-Pleistocene orbital forcing of climate, we calculated the sum power in the $1/25$ – $1/18$ kyr $^{-1}$ (precession), $1/43$ – $1/38$ kyr $^{-1}$ (obliquity), and $1/126$ – $1/89$ kyr $^{-1}$ (eccentricity) frequency bands (ranges after Lisiecki & Raymo, 2007). To account for age model uncertainty in the untuned Dove Basin magnetostratigraphic age model, we analyzed 1,000 of the Undatable age-depth combinations for the Dove Basin stacks and calculated the median value and ± 1 sigma range. To assess how well this uncertainty structure captures amplitude variations in the orbital signal, we calculate an ensemble of magnetostratigraphic age models for IODP Site U1308 using the same methods we used for Sites U1536 and U1537 (Figure S1b). We perform the same time series analysis discussed here on the Site U1308 NGR record on this ensemble of age models and compare those results to time series analysis of Site U1308's LR04 tuned benthic $\delta^{18}\text{O}$ age model (Figure S1a) (Channell et al., 2016; Hodell & Channell, 2016). Choice of undatable *xfactor* in the Dove Basin age models (Lougheed & Obrochta, 2019) controls how much age uncertainty grows between the magnetic reversals (Figure S2a) which influences the uncertainty structure of the analysis described here. To assess the sensitivity of our analysis to *xfactor*, we run our analysis on using age models constructed with three *xfactors* in the range Lougheed and Obrochta (2019) consider realistic, 0.05, 0.1, and 0.3 (Figure S2).

3. Results

3.1. Paleomagnetic Results

3.1.1. Paleomagnetic Data Quality

Detailed demagnetization to 50 mT peak AF of the subset of discrete cubes typically reveals a well-defined ChRM following the removal of the vertical drill string-induced overprint around 5–10 mT peak AF (Figure 2). Predicted inclination based on the geocentric axial dipole hypothesis is about -73.5° . Modern inclination according to the International Geomagnetic Reference Field is about -56° due to the influence

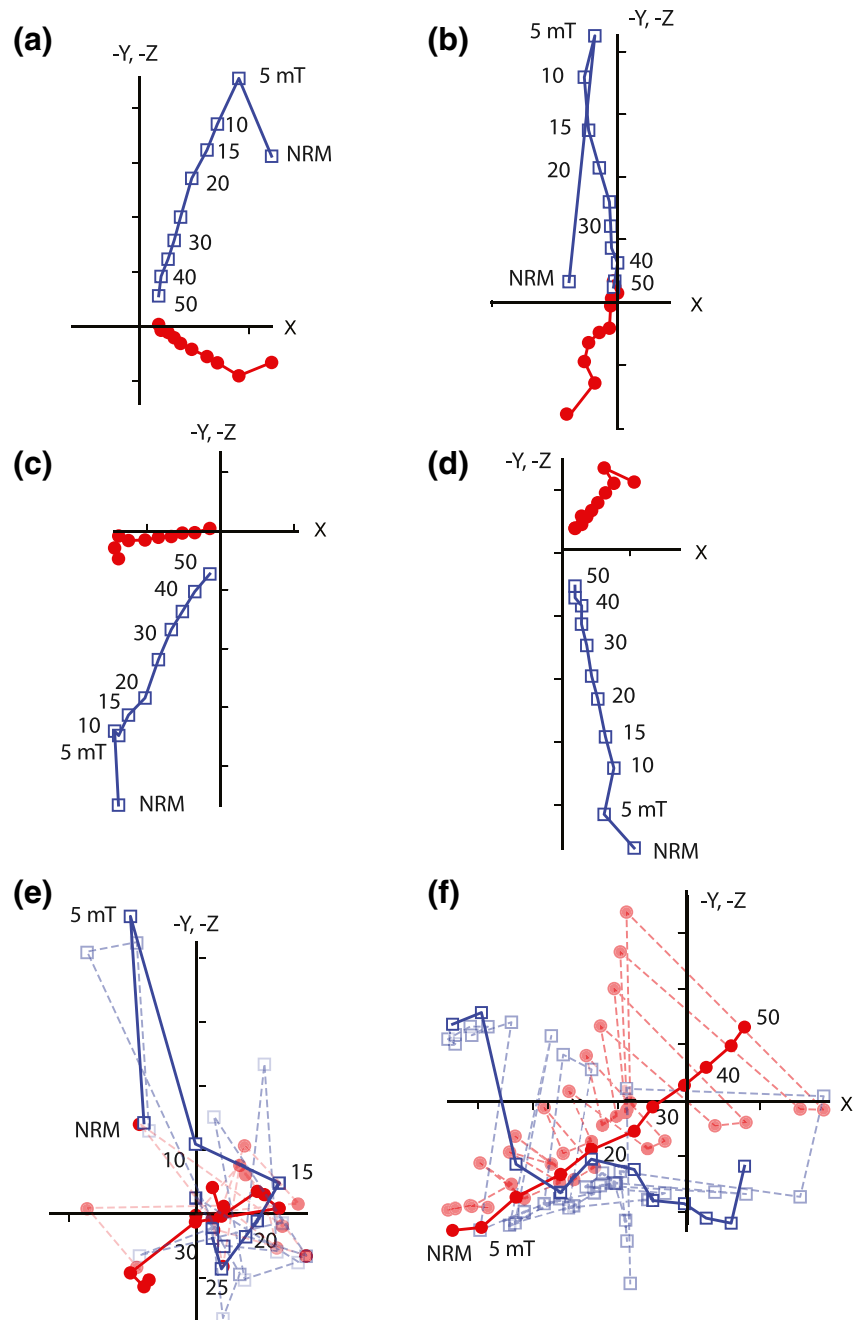


Figure 2. Representative orthogonal projection plots or Zijderveld diagrams (Zijderveld, 1967). All primary demagnetization data are available through the MagIC database (DOI: [10.14379/IODP.PR.382.2019](https://doi.org/10.14379/IODP.PR.382.2019)). (a) U1536A-36F-1W 120–122 cm; NRM = 72 nAm². (b) U1537A-24H-3W 104–106 cm; NRM = 14 nAm². (c) U1536A-39F-3W 80–82 cm; NRM = 94 nAm². (d) U1537A-18H-2W 105–107 cm; NRM = 70 nAm². (e) U1536A-6H-2W 134–136 cm; NRM = 1 nAm². (f) U1537A-5H-3W 110–112 cm; NRM = 32 nAm². Blue open symbols are the vertical projection (x, z), and red closed symbols are the horizontal projection (x, y). For (a–f), darker lines/symbols are the Fischer mean (Fisher, 1953) of all measurements made in the three-axis demagnetization protocol (see Methods). For (e–f), light symbols and stippled lines are the individual measurements made in the three-axis demagnetization protocol. NRM, natural remanent magnetization.

of a region with low total field intensity relative to the geocentric axial dipole and referred to as the South Atlantic Anomaly (Thébault et al., 2015). Examples of typical data with steep vectors consistent with normal and reverse polarity from Sites U1536 and U1537 are presented in Figures 2a–2d.

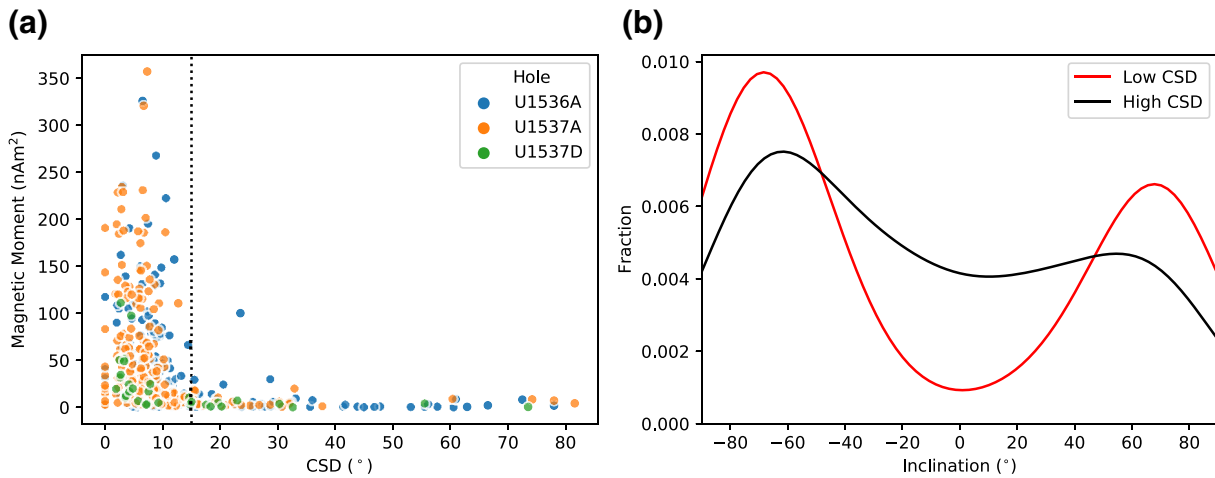


Figure 3. (a) Plot of circular standard deviation (CSD) of measurements at the 15 mT step compared with moment from holes U1536A (blue), U1537A (orange), and U1537D (green). Vertical dashed line denotes CSDs equal to 15°. (b) Kernel density plots of average inclination for the 15 mT step for the data with high CSDs ($>15^\circ$, black line) and those with low CSDs ($\leq 15^\circ$, red line).

While most samples displayed simple demagnetization behavior toward the origin, some discrete data were difficult to interpret. In one case, the sample U1537A-5H-3W, 110–112 cm acquired a remanent magnetization in the presence of the AF, which could be attributed to a spurious ARM or GRM (Figure 2f). In other instances, the magnetic moment of the samples was near or below the practical sensitivity of the SRM and a ChRM could not be isolated (Figure 2e).

Considering these observations, we calculated the circular standard deviation (CSD) of measurements made in the three AF demagnetization positions following 15 mT peak AF. Large CSD values are typically associated with small magnetic moments with only a few samples displaying high CSD and relatively high magnetic moment (Figure 3a). For inclination values following 15 mT peak AF, samples with low CSD values ($\leq 15^\circ$) display a clear bi-model distribution, consistent with normal and reverse distributions centered around geocentric axial dipole like values (Figure 3b). Samples with high CSD values ($>15^\circ$) also have a bimodal distribution; however, the peaks are less pronounced and there are a relatively greater number of shallow inclinations. While it is likely that some intervals are complicated by GRM (e.g., Figure 2f), the majority of poorly defined ChRMs are likely related to small magnetic moments (Figure 3). Discrete data for Site U1537 as a function of depth are plotted in Figure 4i, with closed symbols having CSD values $\leq 15^\circ$ and open symbols having CSD values $> 15^\circ$.

3.1.2. Magnetic Stratigraphy

Archive half and discrete cube measurement inclinations display alternations between intervals with values dominantly consistent with normal or reverse polarity (Figures 4e–4j). Some seemingly anomalous data may be geomagnetic in nature, reflecting geomagnetic excursions; however, potential candidates for these geomagnetic excursions need to be studied in further detail in shore-based paleomagnetic laboratories. More often, there are values that appear anomalous with either shallow inclinations or brief intervals consistent with the opposite polarity that are likely not geomagnetic in nature. Many of these anomalous intervals in archive half data are associated with high magnetic moments, which in some instances could confidently be attributed to the presence of IRD. Other intervals are likely the result of localized coring deformation, which is not reproducible between parallel holes and could be recognized in X-ray images. While on ship, the paleomagnetic and stratigraphic correlator teams worked together to avoid these deformed intervals in the splice. While it is possible to use qualitative criteria derived from X-ray images or paleomagnetic data to improve the visual appearance of the data, we choose to present all data in our figures for this study, outside of data collected within 5 cm from section edges. Ultimately for this study, our discussion uses the reversal

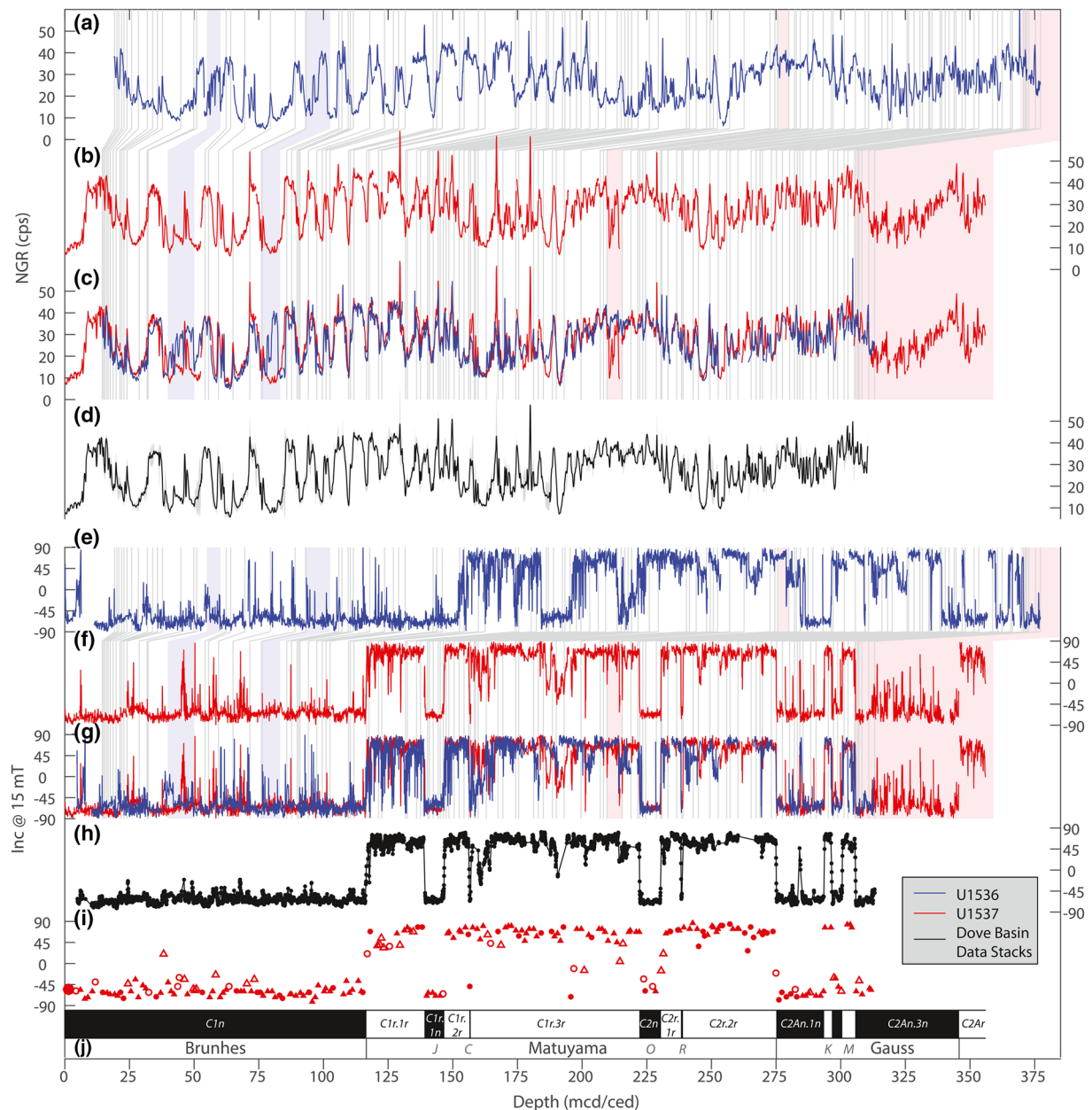


Figure 4. NGR-based correlation of Sites U1536 (blue) and U1537 (red), including (a) data for U1536 on its mcd scale, (b) data for U1537 on its mcd scale, (c) superimposed alignment of the two records on their ced scale, and (d) the Dove Basin NGR stack (black = mean; shading = standard deviation). Gray lines indicate tie points and blue and red shading indicates intervals with common slumping in U1536 and U1537, respectively. Inclination-based magnetic polarity stratigraphy for Dove Basin, including (e) archive half inclination data after 15 mT peak AF for U1536 on its mcd scale (blue), (f) archive half inclination data after 15 mT peak AF for U1537 on its mcd scale (red), (g) superimposed alignment of the two records on their ced scale, and (h) an inclination stack (black) to highlight the common signal. (i) For comparison, the Fisher mean (Fisher, 1953) inclination of U1537 discrete samples after 15 mT peak AF demagnetization in three positions. Triangles indicate data within the splice and circles indicate off-splice data transferred to the mcd scale by their affine offset. Closed symbols indicate circular standard deviations (CSDs) less than 15° while open symbols indicate CSD higher than 15° (see Figure 3). (j) Interpreted magnetic polarity (black = normal; white = reverse) based on the U1537 archive half data and assignment to the geomagnetic polarity timescale (J = Jaramillo; C = Cobb Mountain; O = Olduvai; R = Reunion; K = Kaena; M = Mammoth). AF, alternating field; ced, correlated equivalent depth; GRA, gamma ray attenuation; mcd: meters composite depth; NGR, natural gamma radiation.

positions identified in Site U1537; however, this interpretation is informed through comparisons with discrete cube sample data, visual core descriptions, and X-ray observations (Figures 4e–4j).

Polarity transitions were defined from archive-half data by identifying the closest observation of stable polarity above and below the transitional interval, with stable defined as three consecutive archive half measurements of inclination steeper than $\pm 45^\circ$. If the transition was directly observed in a cored section, we report the top and bottom of that transitional interval and the midpoint of those two values. If the transition was not observed and therefore likely between two cored intervals in a data gap, we report the measurements above and below this data gap and the midpoint of those two values. Polarity transition depths are summarized in Tables S7–S10.

The APC/HLAPC sections of Site U1536 span C1n (Brunhes) to below C2An.2r (Mammoth) in C2An.3n (early Gauss) and include every polarity zone of the Geologic Timescale 2012 (GTS12) (Gradstein et al., 2012) (Figures 4e and 4j). All reversals of the GTS12 in this interval were directly observed in cored intervals except for the top of C2An.1r (Kaena). Archive half inclination data are often noisy, particularly between 150 and 185 mcd in what we interpret to be C1r.1r (late Matuyama) but have primarily reverse (steep positive) inclinations (Figure 4e). Intermediate directions (not consistent with normal or reverse inclinations) are also found during other intervals of the C1r.3r and C2r.2r (middle and early Matuyama) and are not interpreted as polarity transitions. The intervals below the normal (steep negative) inclinations interpreted as C1r.2n (Cobb Mountain) are difficult to interpret and therefore we only assign the top of C1r.2n (Cobb Mountain) and not the base as an age control point in our age model. Despite these issues, the inclination record for U1536 was interpreted independently, before recovery of Site U1537, and is entirely consistent with the interpretation of Site U1537 when the two records are aligned using NGR data, giving us a high degree of confidence in our interpretation (Figure 4g).

The APC/HLAPC sections of Site U1537 can confidently be assigned to include C1n (Brunhes) to C2An.3n (early Gauss) and included every polarity zone of the GTS12 in between (Gradstein et al., 2012) (Figures 4f and 4j). All reversals of the GTS12 in the time interval were directly observed in cored intervals, although the boundaries of C2An.2r (Mammoth) were recovered close to core edges. Below about 287 mbsf in hole D, U1537 recovered predominantly slumped sediments, as identified in visual core descriptions and X-ray images (Figure 4b); however, predominantly reverse magnetized sediments underlay normal magnetized sediments below around 322 mbsf, suggesting the base of APC/HLAPC cored sediments are C2Ar (late Gilbert) in age (Figure 4f). Overall, the archive half inclination record for U1537 is much less noisy than U1536, allowing a clear-cut correlation to the geomagnetic polarity timescale (Figure 4j). In part, this may be related to the extremely calm seas and high-quality core recovery during the drilling of hole U1537A. Like Site U1536, there is an interval of intermediate inclinations (not consistent with normal or reverse polarity) during C1r.3r (middle Matuyama), but unlike Site U1536, these intermediate inclinations are not present in C2r.2r (early Matuyama). These intervals are associated with weak NRM intensities and high CSD values of the discrete sample measurements following 15 mT peak AF demagnetization in three positions (Figure 4i), suggesting we are not resolving the ChRM associated with the geomagnetic field. As in Site U1536, an interval of intermediate inclinations is observed below the normal (steep negative) inclinations that are interpreted as C1r.2n (Cobb Mountain) (Figure 4f). This creates uncertainty in the position of the base of C1r.2n (Cobb Mountain) and leads us to only assign the top as an age control point in our age model.

3.2. Dove Basin Stratigraphic Framework

The NGR records for Sites U1536 and U1537 show remarkable similarity to one another, suggesting that, despite differences in sedimentation rates and slumping at different intervals, the lithostratigraphy of these two sites record regional signals. A total of 118 tie points were used spanning 377.22 mcd at Site U1536 and 313.10 mcd at Site U1537 (Figures 4a–4c). NGR features that do not appear to correlate between sites, particularly two intervals in the upper 100 mcd of U1536 and one interval around 210 mcd in Site U1537, are associated with slump features in the cores, as confirmed by sedimentological descriptions and analysis of X-ray images (Weber et al., 2019), suggesting these slumps are local disturbances. There is excellent agreement between the inclination records of the two sites after alignment based on NGR, supporting the identification of reversal positions relative to the lithostratigraphy (Figure 4g). In addition to confirming the regional nature of the Dove Basin lithologic changes, the core and resulting stack provides a more continu-

ous record in the deeper part of the record, where the composite record for Site U1537 is limited to a single hole and there is missing recovery between core sections.

3.3. Dove Basin Magnetostratigraphic Timescale

The ultimate goal in this study is to make a direct comparison between the orbital signals imprinted in Dove Basin lithostratigraphy, a local record of Antarctic and Southern Ocean dynamics, and benthic $\delta^{18}\text{O}$, a global record of ice volume and deep-sea temperature. Previous studies have often assumed sedimentary physical property within the 41 kyr world varies with a dominant obliquity cycle, in phase with benthic $\delta^{18}\text{O}$, and have tuned accordingly. However, given that at least one hypothesis to explain the 41 kyr world specifically involves climate paced by Southern Hemisphere precession in Antarctica (Raymo et al., 2006), we wanted to test that assumption instead of using it. Therefore, we used an ensemble of untuned (independent) magnetostratigraphic age models in our analysis.

It is difficult to study signals that operate on 19, 23, 41, and ~ 100 kyr periodicities using a magnetostratigraphic age model because of the relatively low number of age-depth tie points that such age models contain. For the last 3.5 Myr, magnetic reversals of the geomagnetic polarity timescale occur on average every 250 kyr, although at irregular intervals, with polarity zone durations ranging from 21 to 774 kyr (Channell et al., 2016). Our magnetostratigraphic age model therefore does not capture variability in sedimentation rates which operate on shorter timescales, such as those which are expected to occur across the alternating deposition of terrigenous and diatomaceous facies.

Given these limitations from our magnetostratigraphic age model, we approach our investigation of these orbital signals with the following strategy. First, despite the low-resolution age model, we can investigate the amplitude modulation of the signal within frequency bands representative of orbital variations over >100 kyr timescales. Second, we can construct an ensemble of a possible age-depth relationships to quantify uncertainty in amplitude modulations given the magnetostratigraphic constraints. Third, we can compare the phasing of the local Dove Basin climate signals to benthic $\delta^{18}\text{O}$ around magnetic reversals, where the relative stratigraphy of reversal positions in our record can be compared to a well-defined reference.

To compare our Dove Basin record with benthic $\delta^{18}\text{O}$, we used the LR04 benthic $\delta^{18}\text{O}$ stack and its astronomically tuned timescale (Lisiecki & Raymo, 2005) and the benthic $\delta^{18}\text{O}$ and paleomagnetic record from North Atlantic IODP Site U1308 (Channell et al., 2008, 2016; Hodell & Channell, 2016; Hodell et al., 2008), a reoccupation of Deep Sea Drilling Program (DSDP) Site 609 (Ruddiman, Kidd, et al., 1987). The high-resolution records of Site U1308 establish the relative stratigraphic relationship between magnetic reversals and benthic $\delta^{18}\text{O}$, allowing for a discussion of climate signal phase relative to the reversals that are not subject to the uncertainties in the LR04 timescale itself (e.g., Ahn et al., 2017; Bajo et al., 2020; Lisiecki & Stern, 2016). The record at Site U1308 extends to the base of C2An.1r (Kaena; ~ 3.1 Ma). But it contains a hiatus around the base of C2r.2r (the Gauss-Matuyama boundary; ~ 2.6 Ma) (Channell et al., 2016). To define the age of the boundaries of C2An.2r (Mammoth; ~ 3.3 – 3.2 Ma) and the base of C2An.3n (early Gauss; ~ 3.6 Ma), we use the LR04 estimates, which are based on the average of estimates from multiple records with various resolution and quality and can have standard deviations that range from 5 to 22 kyr (Lisiecki & Raymo, 2005).

Using Site U1308 to establish the stratigraphic position of the magnetic reversals is important as not all magnetic reversals of other popular timescales, like the current geologic timescale (GTS12), are directly intercalibrated with benthic $\delta^{18}\text{O}$ (e.g., Gradstein et al., 2012; Lourens et al., 1996; Shackleton et al., 1990, 1995). For example, age estimates based on the eastern equatorial Pacific Sites 677 and 846 are derived from records with high quality orbital-resolution benthic $\delta^{18}\text{O}$ data but lack magnetic reversal stratigraphy. Instead, the reversal positions rely on indirect comparisons to other sites from DSDP Leg 94 and Ocean Drilling Program (ODP) Leg 138 (Shackleton et al., 1990, 1995). The GTS12 age estimates from the base of C1n (Brunhes) to C2n (Olduvai) are linked to paired paleomagnetic stratigraphy and benthic $\delta^{18}\text{O}$ from the low-resolution (~ 1.2 cm/kyr) western Philippine Sea Core MD97-2143 (Hornig et al., 2002). GTS12 ages for reversals below C2n (Olduvai) to the base of C2An.3n (early Gauss) are based on the astronomical tuning of lithology and sea surface temperature of Mediterranean sections without benthic $\delta^{18}\text{O}$ (Lourens et al., 1996). We chose to compare the Dove Basin records to the long, high-resolution, and near-continuous records of both magnetic

polarity and benthic $\delta^{18}\text{O}$ at Site U1308, as it can provide a precise relative timing relationship between the two records. However, this approach assumes that the U1308 record is globally representative of all highly resolved magnetic and benthic $\delta^{18}\text{O}$ records. The differences in reversal ages inferred from U1308 and other estimates can be significant, particularly for the age of the base of C2n (Olduvai; ~ 1.9 Ma) which is poorly resolved in many cores (see discussion of Channell et al., 2016, 2020).

Our comparison with orbital curves is timescale dependent and does not consider uncertainty in the orbital solution (in this study, the orbital solution of Laskar et al. [2004] which is nearly identical for the last 10 Myr to the orbital solution of Laskar et al. [1993] used for the LR04 timescale). The LR04 timescale uncertainty is estimated at 4 kyr for 0–1 Ma, 6 kyr from 1 to 3 Ma, and 15 kyr from 3 to 4 Ma (Lisiecki & Raymo, 2005). The LR04 timescale was created using an assumption of how benthic $\delta^{18}\text{O}$ varies relative to a simple nonlinear ice volume model with varying time constant forced by Northern Hemisphere summer insolation (Imbrie & Imbrie, 1980), considering lagged obliquity variations and minimizing sedimentation rate fluctuations of the 57 records that contributed to the stack (Lisiecki & Raymo, 2005). Uncertainty in the LR04 timescale arises from the choice of ice volume model time constant, the tidal dissipation uncertainty in the orbital solution, and unknown changes in Earth's dynamic ellipticity as a result of the ice ages (Laskar et al., 2004; Lisiecki & Raymo, 2005). A recent compilation of astronomically tuned and radiometrically dated Pleistocene magnetic reversals indicates good agreement between the astronomic and radiometric dating methods but with disagreements in the early Pleistocene up to ~ 20 kyr (Channell et al., 2020). Accordingly, while we can discuss the phasing of Dove Basin lithology relative to benthic $\delta^{18}\text{O}$ independent of timescale uncertainty using the relative stratigraphy of the magnetic reversals, phasing relative to the orbital curves has greater uncertainty. However, our discussion of amplitude variations that operate on timescales >100 kyr would be minimally affected by the uncertainties on the order implied by comparison to radiometric dates.

For this study, we assume that magnetic reversals are globally synchronous events; however, it is possible that the directional manifestation and/or duration of magnetic reversals vary based on location (Brown et al., 2007; Clement, 2004; Tauxe et al., 1996). A recent study using high-resolution benthic $\delta^{18}\text{O}$, paleomagnetic measurements, and ^{10}Be in cores from the Indian, Pacific, and Atlantic oceans suggests a 1.6 kyr age uncertainty for the last magnetic reversal relative to the LR04 benthic $\delta^{18}\text{O}$ stack (Valet et al., 2019). An uncertainty of this magnitude could be related to regional differences in the geomagnetic field at low dipole field strengths (Brown et al., 2007), the timescale of $\delta^{18}\text{O}$ mixing in the ocean (Lisiecki & Stern, 2016), uncertainty in ^{10}Be depositional timescales, and/or uncertainty in the graphical correlation (Valet et al., 2019). Similarly, sediment magnetic remanence acquisition processes are poorly understood. Where stratigraphic relationships have allowed for the study of postdepositional remanent magnetizations (pDRMs) (e.g., Egli & Zhao, 2015; Irving & Major, 1964), magnetization signals are estimated to be offset anywhere between 0 and 20 cm in marine sediments (e.g., Channell & Guyodo, 2004; Simon et al., 2018; Stoner et al., 2013; Tauxe et al., 1996). In sediments deposited at sedimentation rates comparable to those observed in Dove Basin, this could result in age offsets up to 4 kyr in the extreme case of a 20 cm pDRM offset and sedimentation rates of 5 cm/kyr. While further constraining such variance is important to understanding the nature of geomagnetic reversals themselves and how sediments record Earth's magnetic field, we consider sedimentation rates in Dove Basin to be sufficiently high. Thus, these uncertainties are small enough, as to not significantly impact our discussion and interpretation of the phasing of orbitally derived signals that operate on timescales of 10 s of kyr.

The resulting magnetostratigraphic age-depth models are tied to the astronomically tuned LR04 timescale but have no tie points beyond the magnetic reversals, providing an age model independent of both biostratigraphic datums (which in some cases are based on earlier magnetic reversal ages whose dates have since been refined) and assumptions about correlation to orbital variability or benthic $\delta^{18}\text{O}$ (Figure 5; Tables S11 and S12). These age models incorporate the uncertainty in depth of each reversal in the age-depth modeling but do not assign age uncertainty estimates for the U1308 benthic $\delta^{18}\text{O}$ calibrated magnetic reversals (to the base of C2A.1r (Kaena; ~ 3.1 Ma), as we are most interested in quantifying relative timing uncertainty compared to the LR04 timescale and not uncertainty associated with the LR04 timescale itself. A ± 5 kyr uncertainty is assigned to the LR04 estimated reversals below the base of C2An.1r (Kaena; ~ 3.1 Ma), for the reasons discussed above.

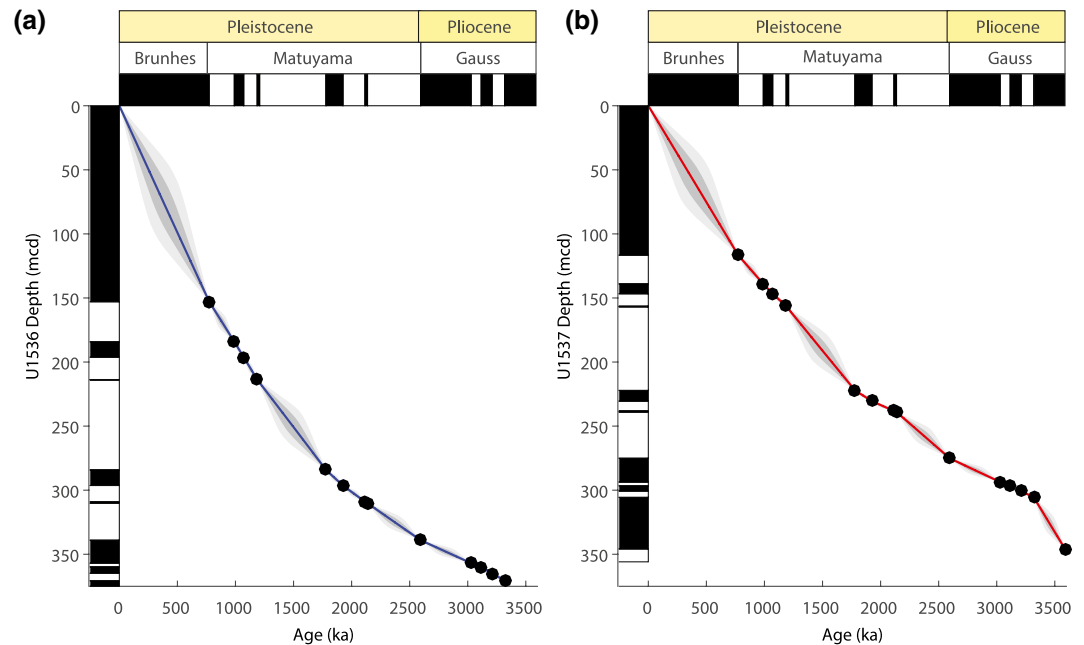


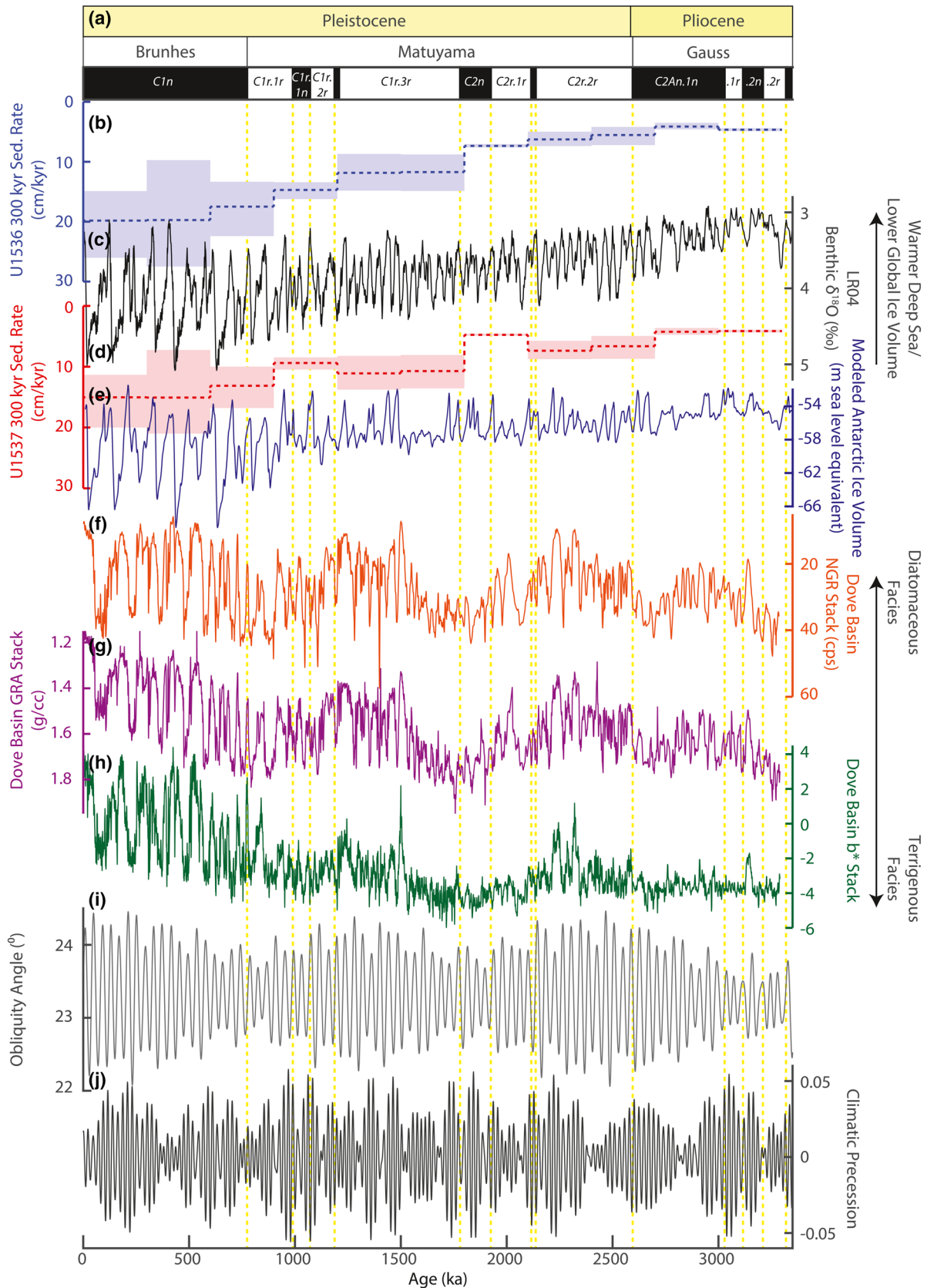
Figure 5. Median age depth models for (a) U1536 (blue) and (b) U1537 (red). Uncertainty is estimated ($\pm 2\sigma$ interval = light gray; $\pm 1\sigma$ interval = darker gray) using Undatable MATLAB tools using an *xfactor* of 0.1 (Lougheed & Obrochta, 2019). Magnetic reversal age control points are black circles. To left of age-depth model is the interpreted magnetostratigraphy for each site and above is the geomagnetic polarity timescale (black = normal; white = reverse).

4. Discussion

4.1. Dove Basin Lithostratigraphy Trends

Age-depth relationships from each site's independent magnetostratigraphy suggest a gradual increase in long-term sedimentation rate over the last ~ 3.3 Myr (Figure 5); however, Site U1537 has higher sedimentation rates near its base during C2An.3n (early Gauss) and C2Ar.1r (late Gilbert) in sediments that have common slump features (Figure 4b). Long-term sedimentation rates, calculated from the median age models over fixed 300-kyr intervals, range from 4 to 5 cm/kyr in C2An.2r-C2An.1n (Mammoth to late Gauss) to 20 cm/kyr in C1n (Brunhes) at Site U1536 and 4 cm/kyr in C2An.2r-C2An.1n (Mammoth to late Gauss) to 15 cm/kyr in C1n (Brunhes) at Site U1537 (Figures 6b and 6d). These changes in sedimentation rate must either be associated with a change in biogenic/lithogenic sediment flux or a change in the sediment focusing factor associated with the dynamics of the contourite. The overall trend in sedimentation rate parallels the long-term trend in globally representative benthic $\delta^{18}\text{O}$ data and modeling of Antarctic ice volume (de Boer et al., 2014) with greater ice volume corresponding to increased sedimentation rates within Dove Basin (Figures 6b–6e).

While our records are not detrended for sediment compaction, there are long wavelength trends in Dove Basin terrigenous (high NGR, high GRA, low b^*) versus diatomaceous (low NGR, low GRA, high b^*) facies in mean values and variance that occur on the timescales of the amplitude modulation of orbital variations (Figures 6f–6j). The ~ 1.2 Myr period in obliquity amplitude modulation has previously been documented in benthic $\delta^{18}\text{O}$, notably in the long-term trends of Oligocene benthic $\delta^{18}\text{O}$, with the coldest intervals correlating to minima in the obliquity amplitude modulation cycle (Pälike et al., 2006). It is also a feature of the amplitude modulation of Miocene to Pleistocene benthic $\delta^{18}\text{O}$ (Lisiecki & Raymo, 2007; Lourens & Hilgen, 1997). Dove Basin sediments display long wavelength trends in the mean values of NGR, GRA, and b^* that coincide with this ~ 1.2 -Myr period from the earliest Pleistocene in C2r.2r (early Matuyama) to at least the middle Pleistocene around C1r.1n (Jaramillo). This includes an extended interval of terrigenous biased facies centered around the ~ 1.8 Ma obliquity amplitude modulation minimum, extending from below to above C2n (Olduvai). Following C1r.1n (Jaramillo), NGR, GRA, and b^* have increased variance and may continue to follow the ~ 1.2 Myr obliquity cycle, with higher mean NGR values (bias to more terrigenous



facies) around the obliquity amplitude modulation minimum ~500 to 900 ka during C1r.1r (late Matuyama) and early C1n (Brunhes) and lower mean NGR values (more diatomaceous facies) during middle to late C1n (Brunhes).

Although the amplitude modulation of obliquity clearly influences the maximum expression of diatomaceous and terrigenous facies in Dove Basin over million-year timescales in the Pleistocene, the long (multi 100 kyr) wavelength trends in late Pliocene NGR, GRA, and b^* do not display as clear a relationship (Figure 6). While NGR and GRA are biased toward higher (terrigenous facies bias) values at the base of our record in C2An.2r (Mammoth) during an obliquity amplitude modulation minimum, there is a distinct minimum (diatomaceous facies bias) in their mean values at ~2.9 Ma in early C2An.1n (late Gauss) and maximum (terrigenous facies bias) ~2.7 Ma in late C2An.1n (late Gauss) that does not follow the ~1.2 Myr obliquity cycle. b^* does not display any long wavelength trends during the late Pliocene C2An (Gauss).

Earth's obliquity angle controls the latitudinal gradient of insolation, with times of low obliquity having an enhanced gradient and increased meridional transport of heat and moisture from low latitudes to the poles (Raymo & Nisancioglu, 2003; Timmermann et al., 2014). Our observations indicate that multimillion-year variations in Dove Basin lithology are sensitive to how extreme these latitudinal gradients are. But we are left with several questions that we investigate in the next sections. Does Dove Basin lithology have clear 41 kyr obliquity pacing in the Pleistocene? Was there a change in how the Antarctic and/or Southern Ocean dynamics that influence Dove Basin lithology respond to orbital forcing around Plio-Pleistocene boundary times and during the MPT? What are the implications for Antarctica's ice sheet evolution?

4.2. Dove Basin Lithostratigraphy Rhythms

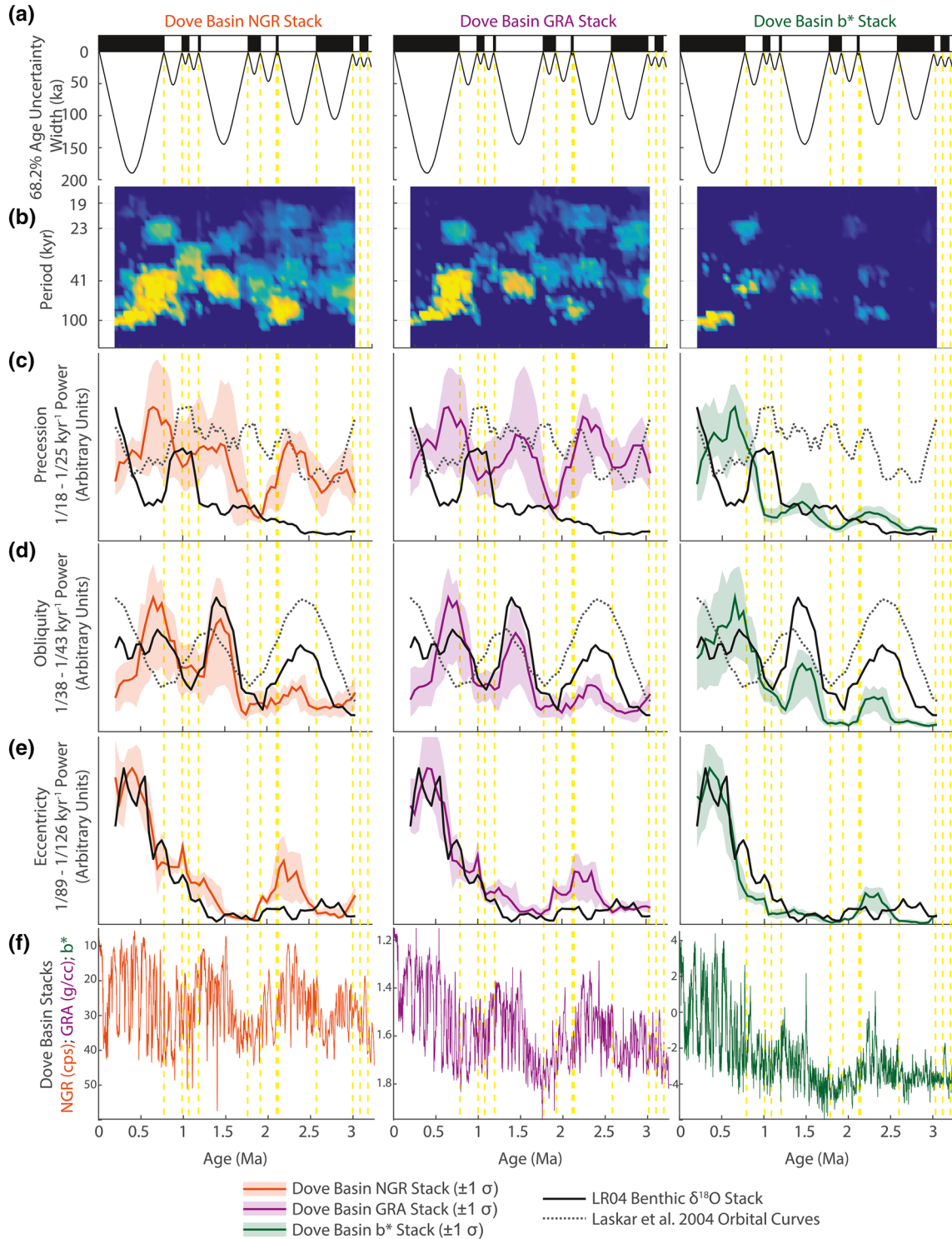
As discussed earlier, it is challenging to investigate orbital periodicities using the lower resolution magnetostratigraphic age model. Accordingly, to address uncertainty related to the resolution of the age model, we discuss the results of an ensemble of analyses on 1,000 possible age-depth relationships generated using Undatable (Figure 7). For each of the significant orbital periods, we compare the orbital solution, LR04, and each of the physical parameters, NGR, GRA, and b^* . We note that the accuracy of our age model relative to the LR04 timescale and benthic $\delta^{18}\text{O}$ will be highest in the immediate vicinity of magnetic reversals (Figure 7a) and degrades to almost ± 200 kyr ($\pm 1\sigma$) in the middle of the Brunhes Chron. Therefore, to build on our understanding of the frequency characteristics of Dove Basin lithostratigraphy, we can use the phasing of local Dove Basin climate signals relative to the magnetic reversals and their positions at North Atlantic Site U1308 relative to benthic $\delta^{18}\text{O}$ (Section 4.3).

4.2.1. Eccentricity Frequency Band

All three Dove Basin parameters, NGR, GRA, and b^* , show a dramatic transition to strong power in the frequency band associated with the ~100 kyr eccentricity cycle roughly coincident with the transition that occurs in benthic $\delta^{18}\text{O}$ (Clark et al., 2006; Lisiecki & Raymo, 2007) known as the MPT (Figure 7e). In Dove Basin, this transition starts around 1.35 Ma, with the approximate midpoint of this transition around 0.65 Ma, and maximum eccentricity strength by 0.4 Ma. The onset of the transition occurs slightly later in b^* relative to NGR, GRA, and benthic $\delta^{18}\text{O}$, likely reflecting the step change in signal amplitude of the b^* record (Figure 6h).

Interestingly, there is an interval with higher power in the eccentric frequency band during the early Pleistocene, with a plateau between 2.1 and 2.4 Ma (Figure 7e). Power in the eccentricity band preceding the MPT has previously been described in a late Pliocene IRD record from east Antarctica, between 2.5 and 3.5 Ma (Patterson et al., 2014) although that record does not extend to the 2.1–2.4 Ma age range. While less than the power observed following the MPT, benthic $\delta^{18}\text{O}$ also shows peaks in eccentricity frequency power centered around 2.7 and 2.1 Ma (Figure 7; Lisiecki & Raymo, 2007). In the Dove Basin record, we suspect

Figure 6. Dove Basin stacked data on their magnetostratigraphic age. (a) Geologic timescale and geomagnetic polarity, (b) long-term sedimentation rate in 300-kyr intervals for Site U1536 calculated from the median age model (blue dashed line) and 68.2% interval (blue shading), (c) LR04 benthic $\delta^{18}\text{O}$ stack (Lisiecki & Raymo, 2005), (d) long-term sedimentation rate in 300-kyr intervals for Site U1537 calculated from the median age model (red dashed line) and 68.2% interval (red shading), (e) modeled Antarctic ice volume (de Boer et al., 2014), (f) Dove Basin NGR stack (orange), (g) Dove Basin GRA stack (purple), (h) Dove Basin b^* stack (green), (i) obliquity angle and (j) climatic precession from Laskar et al. (2004). GRA, gamma ray attenuation; NGR, natural gamma radiation.



two prominent diatomaceous facies intervals during C2r.2r (early Matuyama; ~2.20–2.35 Ma) contribute to this signal (Figures 6f–6h).

4.2.2. Obliquity Frequency Band

Previously, it has been recognized that power in the obliquity frequency band of benthic $\delta^{18}\text{O}$ tracks the ~1.2 Myr cycle in obliquity amplitude modulation from the early Pliocene to about 1.4 Ma, where they decouple (Lisiecki & Raymo, 2007). During the Pleistocene, the power of all three of the Dove Basin lithologic parameters follow the pattern of benthic $\delta^{18}\text{O}$ in the obliquity band, including after 1.4 Ma where obliquity power in benthic $\delta^{18}\text{O}$ decouples from the orbital curve (Figure 7d). However, the relative power increases in the Dove Basin records in each of three successive peaks of the last 3.3 Myr relative to benthic $\delta^{18}\text{O}$ and the orbital curve, with a large increase around 1.6 Ma. The variability in the power in the obliquity frequency band within the Dove Basin records during the early Pleistocene is consistent with the earlier observation of the long-term trends in lithologic parameter mean values tracking the amplitude modulation of the obliquity curve. The initial increase in the Dove Basin lithologic parameters' obliquity power occurs around 2.45 Ma, lagging benthic $\delta^{18}\text{O}$ and the orbital curve and suggesting this strong response to obliquity forcing in Dove Basin lithostratigraphy became important in the early Pleistocene and was not as important in the late Pliocene. Again, this is consistent with the long-term trends in the mean values of the Dove Basin lithologic parameters that suggest the mean expression of diatomaceous versus terrigenous facies is sensitive to the long-term variations in obliquity amplitude modulation during the Pleistocene (Figure 6).

4.2.3. Precession Frequency Band

One of the outstanding questions in paleoclimatology is the reason for modest to absent power in the precession band in benthic $\delta^{18}\text{O}$ during the late Pliocene and early Pleistocene (Raymo & Huybers, 2008; Raymo & Nisancioglu, 2003). However, despite weak power in the precession frequencies, the overall pattern of changes in Plio-Pleistocene benthic $\delta^{18}\text{O}$ power tracks the pattern of changes in the precession forcing but with an exponential increase in power starting around 2.5 Ma (Lisiecki & Raymo, 2007). This suggests that the precession forcing is not absent, but the manifestation of the signal in benthic $\delta^{18}\text{O}$ becomes gradually stronger through the Pleistocene. In the Dove Basin b^* stack, precession power is muted in the late Pliocene and early Pleistocene, with a sharp increase around 0.95 Ma, just slightly preceding the increase in b^* eccentricity power (Figure 7c). Despite the muted signal, there are slight maxima in b^* precession power centered at 1.45 and 2.3 Ma and slight minima at 1.1, 1.9, and 2.7 Ma. The character of the Dove Basin NGR and GRA stacks is surprisingly different, showing high power in the precession frequencies from 3.3 to 2.1 and 1.5 to present relative to b^* and LR04. NGR and GRA also show relative minima in precession power at around 1.0, 1.9, and 2.7 Ma. While some of these maxima and minima roughly align with maxima and minima in the orbital curve, there is not a clear relationship between NGR, GRA, and the orbital curve that is consistent throughout the record. However, maxima in precession power roughly coincide with peaks in obliquity power in the Pleistocene, which might indicate times of increased sensitivity to orbital forcing for the factors that control Dove Basin sedimentation.

4.3. Implications for Plio-Pleistocene Ice Sheet Histories

The long-term trends in the mean values of the Dove Basin stacks do not seem to follow the Plio-Pleistocene trend toward greater ice volume (Figure 6e); during the Pleistocene, however, alternation of Dove Basin's terrigenous and diatomaceous facies shows power in the ~1/100 kyr⁻¹ eccentricity and 1/41 kyr⁻¹ obliquity fre-

Figure 7. Comparison of the spectral power of Dove Basin data stacks. (a) Width of the 68.2% age model uncertainty calculated using Undatable and an *xfactor* of 0.1 (Lougheed & Obrochta, 2019) and the geomagnetic polarity timescale (black = normal; white = reverse). (b) Spectral power of the Dove Basin data stacks above the 85% confidence interval calculated using the multitaper method (dark blue = low power; yellow = high power). (c–e) Spectral power (scaled to maximum value) of the Dove Basin data stacks (NGR = orange; GRA = purple; b^* = green; line = median; shading = ± 1 sigma range from the ensemble of calculated magnetostratigraphic age models (Figure 5), the LR04 benthic $\delta^{18}\text{O}$ stack (solid black line; Lisiecki & Raymo, 2005), and the Laskar et al. (2004) (dashed line) orbital parameters for (c) climatic precession and (d) obliquity angle. (e) Power in frequencies associated with Earth's precession (1/18–1/25 kyr⁻¹), (d) power in the frequency associated with Earth's obliquity (1/38–1/43 kyr⁻¹), and (e) power in the frequency associated with Earth's eccentricity (1/89–1/126 kyr⁻¹). (f) The NGR, GRA, and b^* stacks are plotted for comparison. Uncertainty estimates in (c–e) are dependent on the choice of *xfactor*. Figure S2 compares these uncertainty estimates to the upper and lower range of *xfactor* values Lougheed and Obrochta (2019) indicate may be realistic. GRA, gamma ray attenuation; NGR, natural gamma radiation.

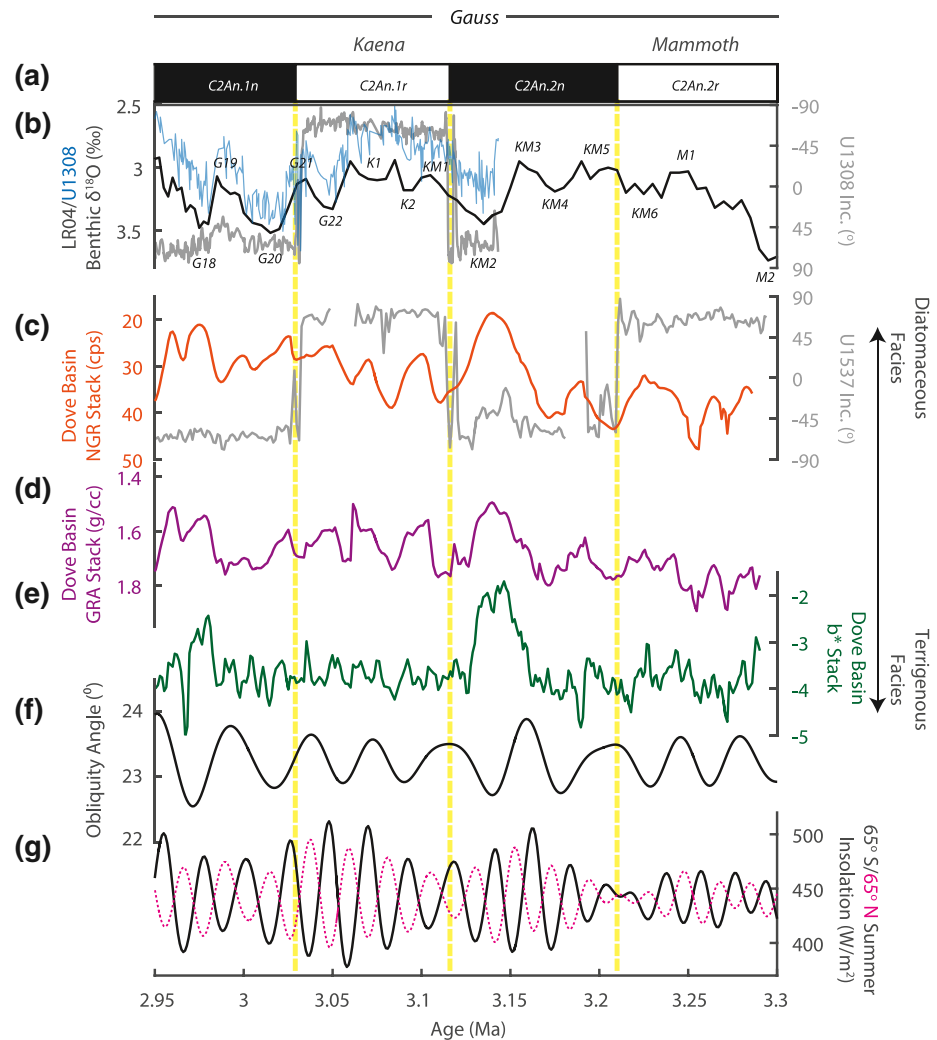


Figure 8. Pliocene subchrons of the Gauss Chron. (a) Geomagnetic polarity timescale (black = normal; white = reverse). (b) The LR04 benthic $\delta^{18}\text{O}$ stack (black; Lisiecki & Raymo, 2005), U1308 benthic $\delta^{18}\text{O}$ (blue; Hodell & Channell, 2016), and U1308 inclination (gray; Channell et al., 2016). U1308 $\delta^{18}\text{O}$ is scaled by 1.11 for comparison to the LR04 curve. Marine isotope stages are labeled. (c) Dove Basin NGR stack (orange) and U1537 inclination (gray). (d) Dove Basin GRA stack (purple). (e) Dove Basin b^* stack (green). (f) Obliquity angle (black) and (g) summer insolation calculated for January 21 at 65°S (black) and July 21 at 65°N (stippled pink) (Laskar et al., 2004). Magnetic reversals used as age control points are marked by the vertical yellow lines. Note that Site U1308 is used to establish the direct stratigraphic relationship between the Kaena magnetic reversals and benthic $\delta^{18}\text{O}$. The relationship between the magnetic reversals and the orbital curves does not have a direct stratigraphic relationship and is timescale dependent. GRA, gamma ray attenuation; NGR, natural gamma radiation.

quencies that are similar to the amplitude modulation and evolution of benthic $\delta^{18}\text{O}$ records (Figures 7d and 7e). Thus, like benthic $\delta^{18}\text{O}$ (cf., Lisiecki & Raymo, 2007), Dove Basin lithostratigraphy displays a proportional response to obliquity forcing during the early Pleistocene, until ~ 1.4 Ma. However, unlike benthic $\delta^{18}\text{O}$, Dove Basin lithological parameters do not appear to relate to obliquity forcing in the late Pliocene. After ~ 1.4 Ma, power in the Dove Basin lithostratigraphy obliquity frequency band follows benthic $\delta^{18}\text{O}$ and not the amplitude modulation of Earth's obliquity angle. At the same time, power in the eccentricity frequency band of the lithologic parameters increases along with benthic $\delta^{18}\text{O}$, which cannot be attributed to direct orbital forcing and probably reflects a nonlinear response in ice sheet behavior (e.g., Imbrie & Imbrie, 1980).

Given this close relationship between Dove Basin lithostratigraphy and benthic $\delta^{18}\text{O}$ in the obliquity and eccentricity bands, it is interesting to see a significantly stronger precession signal in the late Pliocene

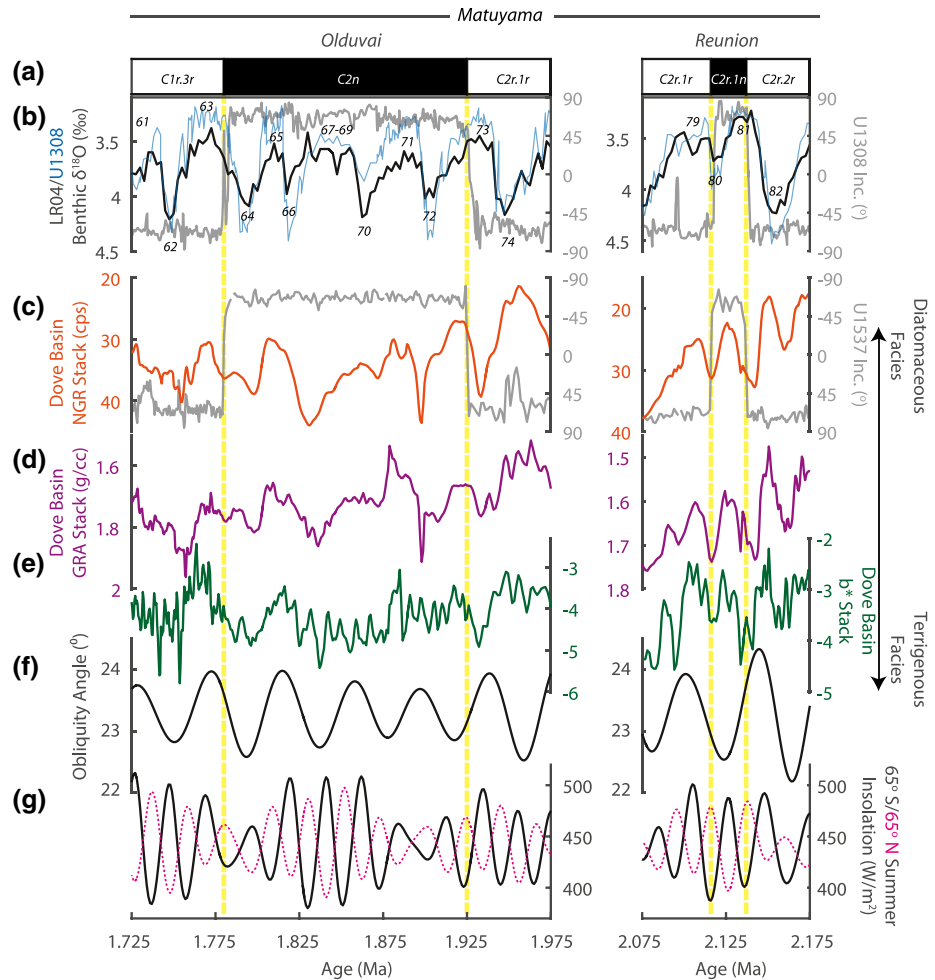


Figure 9. Early Pleistocene subchrons of the Matuyama. (a) Geomagnetic polarity timescale (black = normal; white = reverse). (b) The LR04 benthic $\delta^{18}\text{O}$ stack (black; Lisiecki & Raymo, 2005), U1308 benthic $\delta^{18}\text{O}$ (blue; Hodell & Channell, 2016), and U1308 inclination (gray; Channell et al., 2016). U1308 $\delta^{18}\text{O}$ is scaled by 1.11 for comparison to the LR04 curve. Marine isotope stages are labeled. (c) Dove Basin NGR stack (orange) and U1537 inclination (gray). (d) Dove Basin GRA stack (purple). (e) Dove Basin b^* stack (green). (f) Obliquity angle (black) and (g) summer insolation calculated for January 21 at 65°S (black) and July 21 at 65°N (stippled pink) (Laskar et al., 2004). Magnetic reversals used as age control points are marked by the vertical yellow lines. Note that Site U1308 is used to establish the direct stratigraphic relationship between the magnetic reversals and benthic $\delta^{18}\text{O}$. The relationship between the magnetic reversals and the orbital curves does not have a direct stratigraphic relationship and is timescale dependent. GRA, gamma ray attenuation; NGR, natural gamma radiation.

and early Pleistocene (Figure 7c). The Antiphase Hypothesis (Raymo et al., 2006) predicts that the out-of-phase response of Northern and Southern Hemisphere ice sheets to each hemisphere's summer insolation would hide precession signals apparent in ice sheet proximal records in benthic $\delta^{18}\text{O}$ through destructive interference (e.g., Moree et al., 2021). Thus, if Dove Basin's lithostratigraphy reflects processes that change alongside Antarctica's ice sheet history, we would expect to see precession pacing during the "41 kyr world" that is in phase with Southern Hemisphere summer insolation and not represented in benthic $\delta^{18}\text{O}$.

The strong precession signal in the late Pliocene and delayed onset of obliquity power until the early Pleistocene observed in Dove Basin suggests a change in the nature of the Antarctic Ice Sheet and/or Southern Ocean dynamics along with the inception of significant Northern Hemisphere ice sheets. We investigate these orbital signals further in the intervals around magnetic reversals and subchrons, where our age control is strongest (a summary of the fundamental observations is given in Table S14). As discussed earlier, the stratigraphic position of magnetic reversals relative to benthic $\delta^{18}\text{O}$ is well characterized through direct

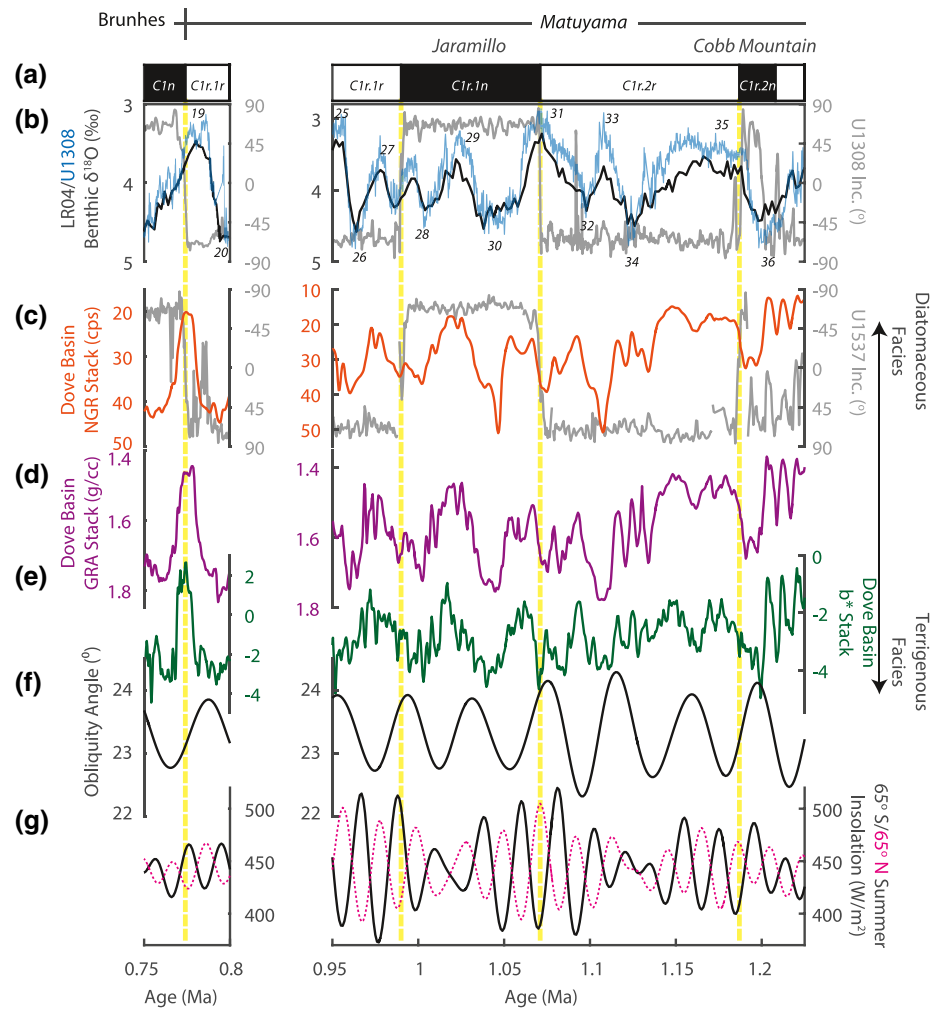


Figure 10. Middle Pleistocene subchrons of the Matuyama and the Matuyama-Brunhes boundary. (a) Geomagnetic polarity timescale (black = normal; white = reverse). (b) The LR04 benthic $\delta^{18}\text{O}$ stack (black; Lisiecki & Raymo, 2005), U1308 benthic $\delta^{18}\text{O}$ (blue; Hodell et al., 2008), and U1308 inclination (gray; Channell et al., 2008). U1308 $\delta^{18}\text{O}$ is scaled by 1.11 for comparison to the LR04 curve. Marine isotope stages are labeled. (c) Dove Basin NGR stack (orange) and U1537 inclination (gray). (d) Dove Basin GRA stack (purple). (e) Dove Basin b^* stack (green). (f) Obliquity angle (black) and (g) summer insolation calculated for January 21 at 65°S (black) and July 21 at 65°N (stippled pink) (Laskar et al., 2004). Magnetic reversals used as age control points are marked by the vertical yellow lines. Note that Site U1308 is used to establish the direct stratigraphic relationship between the magnetic reversals and benthic $\delta^{18}\text{O}$. The relationship between the magnetic reversals and the orbital curves does not have a direct stratigraphic relationship and is timescale dependent. GRA, gamma ray attenuation; NGR, natural gamma radiation.

comparison at IODP Site U1308 in the North Atlantic down to the base of C2An.1r (Kaena), excluding the top of C2An.1n (the Gauss-Matuyama reversal) which occurs around a hiatus (Figures 8b, 9b, and 10b; Channell et al., 2016, 2008). Thus, comparison of the variations in Dove Basin lithology and benthic $\delta^{18}\text{O}$ relative to magnetic reversals is robust to timescale uncertainties; however, comparison of these signals to orbital curves, which do not have a direct stratigraphic relationship with the magnetic reversals, has significant uncertainty.

In the late Pliocene, the base of C2An.1r (Kaena), ~ 3.1 Ma, is found during the transition from the significant glacial MIS KM2 to muted interglacial MIS KM1 at Site U1308 (Figure 8b). In our Dove Basin stacks, the reversal is recorded during a transition from a prominent diatomaceous facies to a terrigenous facies, the opposite of the transition observed in benthic $\delta^{18}\text{O}$ (Figures 8b–8e). Three diatomaceous facies intervals, particularly well resolved in GRA, are observed during C2An.1r (Kaena) (Figure 8d). The top of C2An.1r

(Kaena), ~3.0 Ma, is found in a moderate relatively terrigenous Dove Basin facies, while it is clearly in the interglacial MIS G21 at Site U1308 (compare Figures 8b, 8c–8e). The amplitude of these features in NGR in Dove Basin is greater in the early part of C2An.1r (Kaena) than at the top, while the opposite is true for the variations in benthic $\delta^{18}\text{O}$. On the LR04 timescale, the lower C2An.1r (Kaena) reversal at U1308 is placed in a 65°S summer insolation maxima (Figure 8g), which is consistent with the age reported for the Lourens et al. (1996) timescale, based on lithologic variations that show strong precession variability. However, on this latter timescale, the uncertainty of the reversal age relative to the timescale is around a full precession cycle based on the resolution of the paleomagnetic samples (Zachariasse et al., 1989, 1990). Shackleton et al. (1995) place the reversal in 65°S summer insolation minima based on precession-paced eastern equatorial Pacific carbonate cycles and continuous archive half paleomagnetic measurements, which seems to be more consistent with its position in a terrigenous facies interval in Dove Basin. All three timescales have three 65°S summer insolation maxima between the C2An.1r (Kaena) reversals, consistent with the three diatomaceous facies intervals in the Dove Basin C2An.1r (Kaena) interval. We consider these observations as support for Scotia Sea climate signal changes at precession frequencies driven by peak Southern Hemisphere summer insolation during the late Pliocene, particularly during early C2An.1r (Kaena) (see also Figure S3). If these lithologic changes are related to Antarctic Ice Sheet history, changes in Antarctic ice volume at this time would be muted in the globally integrated benthic $\delta^{18}\text{O}$ signal as small Northern Hemisphere ice sheets, known to be present based on IRD in the northern North Atlantic (e.g., Blake-Mizen et al., 2019; Jansen et al., 2000) wax and wane out of phase, in response to Northern Hemisphere summer insolation. The next question is whether such an antiphased Southern Hemisphere climate signal is observed during the post-2.7 Ma proper 41-kyr world?

To answer this question, we examined the short C2r.1n (Reunion) Subchron, ~2.1 Ma, in the early Pleistocene (Figure 9). We observe a similar out of phase of climatic signal between the Dove Basin and benthic $\delta^{18}\text{O}$ as described above around the C2An.1r (Kaena) Subchron. In the Site U1308 stratigraphy, the base of C2r.1n (Reunion) is found during interglacial MIS 81 and, at the top, near the end of glacial MIS 80 (Figure 9b). In our Dove Basin stack, the base and top of the subchron are associated with terrigenous facies with a diatomaceous facies interval between (Figures 9c–9e). On the LR04 age model, the base and top of C2r.1n (Reunion) are centered in 65°S summer insolation minima, consistent with Antarctic and/or Southern Ocean change at precession frequencies driven by peak Southern Hemisphere summer insolation (Figures 9c–9g). Again, the muted expression of precession in benthic $\delta^{18}\text{O}$ would be consistent with Northern Hemisphere and Antarctic ice volume signals occurring out of phase with each other (e.g., Raymo et al., 2006), if Dove Basin lithology is a reflection of Antarctic Ice Sheet evolution.

Next, the C2n (Olduvai) Subchron at ~1.8–1.9 Ma is within the previously discussed interval of low power in Dove Basin and benthic $\delta^{18}\text{O}$ obliquity and precession frequencies which suggests low sensitivity to orbital forcing (Figure 7), low amplitude modulation of the obliquity angle, and bias toward Dove Basin terrigenous facies (Figure 6). At high resolution, do the trends observed track Northern Hemisphere or Southern Hemisphere insolation forcing? The base of C2n (Olduvai) is associated with the end of peak interglacial MIS 73 at Site U1308 (Figure 9b) and with the onset of a diatomaceous facies interval at Dove Basin (Figures 9c–9e), indicating an offset, but not a clear out-of-phase relationship between the climate records at each site. The top of C2n (Olduvai) is found at the transition from glacial MIS 64 to interglacial 63 at Site U1308 and at the transition from a terrigenous to diatomaceous Dove Basin facies, suggesting that the climatic signals recorded at the two sites are more or less in phase at this point. These observations do not indicate a strong Southern Hemisphere precession signal around C2n (Olduvai) and seem consistent with benthic $\delta^{18}\text{O}$. However, there is perhaps a weak precession signal seen in NGR and GRA at the top of C2n (Olduvai) and the position of the reversal at the base of C2n (Olduvai) relative to Dove Basin lithologic changes is offset to the reversal's position relative to benthic $\delta^{18}\text{O}$. We suspect that the low sensitivity to orbital forcing (Figure 7) and bias toward terrigenous facies (Figure 6) in Dove Basin lithostratigraphy during C2n (Olduvai) reflects the low amplitude modulation of obliquity forcing. Low obliquity angles result in greater gradients between the amount of insolation at low versus high latitudes, which would drive higher atmospheric transport from low latitudes carrying heat and moisture (Raymo & Nisancioglu, 2003; Timmermann et al., 2014). We hypothesize this represents an interval of net accumulation relative to ablation for the Antarctic Ice Sheet creating a large and relatively stable ice sheet. This would be consistent with evidence for larger Antarctic ice volume during periods of low obliquity amplitude modulation during the

Oligocene (Pälike et al., 2006), although more work is needed to investigate the relationship between Dove Basin lithology and Antarctic ice volume.

Finally, during C1r (late Matuyama), the top of C1r.2n (Cobb Mountain), ~1.2 Ma, occurs at the transition from glacial MIS 36 to interglacial MIS 35 at Site U1308 and at the transition from a terrigenous to a diatomaceous facies in Dove Basin (Figures 10b–10e). The top of C1r.1r (Jaramillo), ~1.0 Ma, is found above an interstadial feature during MIS 28, like the muted diatomaceous facies interval, it is found above in Dove Basin (Figures 10b–10e). The top of C1r.1r (the Matuyama-Brunhes reversal), ~0.8 Ma, is found during the interglacial MIS 19 at U1308 and in a diatomaceous facies interval in Dove Basin (Figures 10b–10e). While these three reversals suggest Dove Basin lithology is responding in phase with benthic $\delta^{18}\text{O}$, the base of C1r.1n (Jaramillo), ~1.1 Ma, is found during the peak of interglacial MIS 31 in U1308 while it is found near the end of a Dove Basin terrigenous facies interval at both U1536 and U1537 (Figures 10b–10e; Figure S4). This reversal is associated with a Northern Hemisphere summer insolation maximum and Southern Hemisphere insolation minimum (Figure 10g). The association of the base of the C1r.1n (Jaramillo) with a colder interval in subantarctic sediments was previously observed by Scherer et al. (2008) at ODP Site 1094, near Bouvet Island, southeastern Atlantic. We consider this consistency between the subantarctic record to be additional support for out-of-phase precession forcing of Antarctica and/or Southern Ocean climate during MIS 31. We hypothesize, based on these four reversals, that the mode shift in orbital forcing of Pleistocene ice sheets that began around 1.4 Ma represents the start of the gradual synchronization of the orbital pacing of Northern and Southern Hemisphere ice sheets, as previously proposed by Raymo et al. (2006), with a brief return to out-of-phase precession signals during the maximum in precession amplitude modulation near the base of C1r.1r (Jaramillo). However, this interval will need to be studied in greater detail with multiple proxies to validate this notion.

5. Conclusion

Drill cores recovered from Dove Basin during IODP Expedition 382 are special archives, containing near-continuous recovery with exceptional magnetostratigraphy and strong orbital variation in lithostratigraphy. This provides the opportunity to study Antarctic Ice Sheet and Southern Ocean responses to orbital forcing on an age model independent of tuning and the associated assumptions that may compromise the validity of interhemispheric comparisons. While the resolution of the magnetostratigraphic model is lower than that of the orbital periods we investigate here, it is used to study the amplitude modulation of important orbital frequency bands (Figures S1 and S7) and to make stratigraphic comparisons with benthic $\delta^{18}\text{O}$ changes around magnetic reversals (Figures 8–10). During the Pleistocene, the amplitude evolution of the obliquity and eccentricity frequency bands of lithologic parameters within Dove Basin are comparable to those exhibited by benthic $\delta^{18}\text{O}$ records (Figures 7d and 7e). During the late Pliocene and early Pleistocene, power in the precession frequency bands of lithologic parameters in Dove Basin is greater than that found in benthic $\delta^{18}\text{O}$ relative to the late Pleistocene (Figure 7c). During some intervals of the late Pliocene and early Pleistocene, these precession signals are in phase with Southern Hemisphere, rather than Northern Hemisphere, summer insolation (Figures 8–10).

If, as is the case for the last glacial cycle (Weber et al., 2012), Dove Basin lithologic changes reflect Antarctic Ice Sheet evolution, the precession paced variations in the late Pliocene and early Pleistocene indicate that Antarctic Ice Sheet changes were sensitive to Southern Hemisphere summer insolation. Within the framework of the antiphase hypothesis, the reason these precession signals are missing in global ice volume signals such as benthic $\delta^{18}\text{O}$ is these Antarctic ice volume changes vary out of phase with precession-paced ice variations in the Northern Hemisphere, for which there is some evidence based on runoff to the Gulf of Mexico (Shakun et al., 2016). Regardless, the frequency character of the Dove Basin record and the position of magnetic reversals around the C2An.1r (Kaena) and C2r.1n (Reunion) Subchrons provide evidence of local summer insolation control of Antarctic and/or Southern Ocean regional climate at least during intervals of the late Pliocene and early Pleistocene (Figures 8 and 9).

We also propose that transitions in the Antarctic Ice Sheet and/or the Southern Ocean occurred around the Plio-Pleistocene boundary and around 1.6 Ma where the amplitude modulation of the obliquity frequency in Dove Basin lithology increases (Figure 7d). Following the Plio-Pleistocene boundary, long-term trends

in the mean diatomaceous versus terrigenous Dove Basin facies are driven by the amplitude modulation of obliquity (Figures 6e–6h). Intervals of lower obliquity amplitude modulation when latitudinal insolation gradients are less variable, like the minimum around 1.8 Ma, may have led to greater meridional moisture transport and higher accumulation relative to ablation in Antarctica. These intervals could indicate times of greater ice sheet stability and/or lower sensitivity to orbital forcing. This is supported by the long-term trends in the Dove Basin record, frequency character of the Dove Basin record, and position of the magnetic reversals around C2n (Olduvai) (Figures 6e–6h, 7d, and 9).

Lastly, the synchronization of Northern and Southern Hemisphere climate began as a gradual process around 1.4 Ma, as previously proposed by Raymo et al. (2006). This trend is expressed here by the change in the frequency characteristic of Dove Basin lithology and benthic $\delta^{18}\text{O}$ relative to orbital forcing and the position of the magnetic reversals between the top of C1r.1r (the Matuyama-Brunhes reversal) and the top of C1r.2n (Cobb Mountain). However, as previously observed by Scherer et al. (2008), during a precession amplitude modulation maximum around the base of C1r.1n (Jaramillo), the hemispheres are notably out of phase (Figures 10 and Figure S4).

Ultimately, the magnetostratigraphic constraints on the trends and rhythms of Dove Basin lithostratigraphy raise new questions for our quest to understand the Plio-Pleistocene evolution of the Antarctic Ice Sheet and its interactions with global climate. For example, what processes drove changes in the frequency characteristics of the Dove Basin record around the Plio-Pleistocene boundary and MPT? What other records from the Northern Hemisphere could show similar precession-paced climate variations in the late Pliocene and early Pleistocene? And, why are long-term trends in the expression of diatomaceous and terrigenous facies linked to the long-term amplitude modulation of obliquity? NGR, GRA, and b^* are tracers of lithologic variability and are convolved signals depending on Antarctica's ice sheet history, dynamics of contourite deposition, primary productivity, and sediment supply. Orbital forcing could operate on one or more of these processes. Moving forward, tracers of ocean circulation, sea surface conditions, and ice sheet discharge will be essential for understanding climate evolution on these timescales. In addition, novel chronologic methods that are independent of sediment lithology and regional paleoenvironment, such as relative paleomagnetic intensity, are needed to more tightly constrain the chronology of the late Pliocene and early Pleistocene.

Acknowledgments

The authors are grateful to the captain, crew, and IODP staff that made IODP Expedition 382 successful. All samples and data were provided by IODP. The authors thank J. Channell for providing U1308 paleomagnetic data. B. Reilly thanks the Scripps Institution of Oceanography for support. US participants on Expedition 382 acknowledge support from the US Science Support Program and Columbia University (National Science Foundation [NSF] award OCE 1450528). L. Tauxe acknowledges support from NSF award EAR 1547263. T. Williams acknowledges support from the IODP JRSO (NSF award 1326927). I. Bailey thanks the Natural Environmental Research Council for financial support for his participation in IODP Exp. 382 (UK IODP Grant NE/T006609/1) and acknowledges additional support from the EU project MARINEFF (Interreg VA France-(Channel)-England Programme project #162). L. F. Pérez has received funding from the Marie Skłodowska-Curie grant agreement No 792773 WAMSISE and the UK-IODP program through the grant NEB1782. F. S. Hoem acknowledges funding through NOW Polar Programs grant ALW.2016.001. L. Armbrecht thanks the Australia-New Zealand IODP Consortium (ANZIC) for their support. We thank Lorraine Lisiecki and Lucas Lourens for insightful reviews of this manuscript.

Data Availability Statement

Sites U1536 and U1537 paleomagnetic data are archived through the MagIC Database (DOI: <http://doi.org/10.14379/IODP.PR.382.2019>). Stratigraphic data are archived in the IODP community at Zenodo.org along with shipboard expedition data (DOI: <http://doi.org/10.5281/zenodo.3776573>). Data and information needed to use the composite depth scales, correlated equivalent depth scales, and age models are included in the supplementary tables.

References

- Acton, G. D., Morris, A., Musgrave, R. J., Zhao, X. X., & IODP SRM Personnel. (2017). *Assessment of the new superconducting rock magnetometer (SRM) on the JOIDES resolution* (IODP technical report). International Ocean Discovery Program.
- Ahn, S., Khider, D., Lisiecki, L. E., & Lawrence, C. E. (2017). A probabilistic Pliocene–Pleistocene stack of benthic $\delta^{18}\text{O}$ using a profile hidden Markov model. *Dynamics and Statistics of the Climate System*, 2(1), dzx002. <https://doi.org/10.1093/climsys/dzx002>
- Anderson, J. B., & Andrews, J. T. (1999). Radiocarbon constraints on ice sheet advance and retreat in the Weddell Sea, Antarctica. *Geology*, 27(2), 179–182. [https://doi.org/10.1130/0091-7613\(1999\)027<0179:RCOISA>2.3.CO;2](https://doi.org/10.1130/0091-7613(1999)027<0179:RCOISA>2.3.CO;2)
- Austermann, J., Pollard, D., Mitrovica, J. X., Moucha, R., Forte, A. M., DeConto, R. M., et al. (2015). The impact of dynamic topography change on Antarctic ice sheet stability during the mid-Pliocene warm period. *Geology*, 43(10), 927–930. <https://doi.org/10.1130/G36988.1>
- Bailey, I., Hole, G. M., Foster, G. L., Wilson, P. A., Storey, C. D., Trueman, C. N., & Raymo, M. E. (2013). An alternative suggestion for the Pliocene onset of major northern hemisphere glaciation based on the geochemical provenance of North Atlantic Ocean ice-rafted debris. *Quaternary Science Reviews*, 75, 181–194. <https://doi.org/10.1016/j.quascirev.2013.06.004>
- Bajo, P., Drysdale, R. N., Woodhead, J. D., Hellstrom, J. C., Hodell, D., Ferretti, P., et al. (2020). Persistent influence of obliquity on ice age terminations since the Middle Pleistocene transition. *Science*, 367(6483), 1235–1239. <https://doi.org/10.1126/science.aaw1114>
- Bakker, P., Clark, P. U., Golledge, N. R., Schmittner, A., & Weber, M. E. (2016). Centennial-scale Holocene climate variations amplified by Antarctic Ice Sheet discharge. *Nature*, 541, 72–76. <https://doi.org/10.1038/nature20582>
- Blake-Mizen, K., Hatfield, R. G., Stoner, J. S., Carlson, A. E., Xuan, C., Walczak, M., et al. (2019). Southern Greenland glaciation and Western Boundary Undercurrent evolution recorded on Eirik Drift during the late Pliocene intensification of Northern Hemisphere glaciation. *Quaternary Science Reviews*, 209, 40–51. <https://doi.org/10.1016/j.quascirev.2019.01.015>

- Blum, P. (1997). *Physical properties handbook: A guide to the shipboard measurement of physical properties of deep-sea cores (ODP Tech note: 26)*. International Ocean Discovery Program.
- Brown, M. C., Holme, R., & Bargery, A. (2007). Exploring the influence of the non-dipole field on magnetic records for field reversals and excursions. *Geophysical Journal International*, *168*(2), 541–550. <https://doi.org/10.1111/j.1365-246X.2006.03234.x>
- Budge, J. S., & Long, D. G. (2018). A comprehensive database for Antarctic Iceberg tracking using scatterometer data. *IEEE Journal of Selected Topics in Applied Earth Observations and Remote Sensing*, *11*(2), 434–442. <https://doi.org/10.1109/JSTARS.2017.2784186>
- Channell, J. E. T., & Guyodo, Y. (2004). The Matuyama Chronozone at ODP Site 982 (Rockall Bank): Evidence for Decimeter-Scale Magnetization Lock-In Depths. In J. E. T. Channell, D. V. Kent, W. Lowrie, & J. G. Meert (Eds.), *Timescales of the paleomagnetic field* (pp. 205–219). Washington, DC: American Geophysical Union.
- Channell, J. E. T., Hodell, D. A., & Curtis, J. H. (2016). Relative paleointensity (RPI) and oxygen isotope stratigraphy at IODP Site U1308: North Atlantic RPI stack for 1.2–2.2 Ma (NARPI-2200) and age of the Olduvai Subchron. *Quaternary Science Reviews*, *131*, 1–19. <https://doi.org/10.1016/j.quascirev.2015.10.011>
- Channell, J. E. T., Hodell, D. A., Xuan, C., Mazaud, A., & Stoner, J. S. (2008). Age calibrated relative paleointensity for the last 1.5 Myr at IODP site U1308 (North Atlantic). *Earth and Planetary Science Letters*, *274*, 59–71.
- Channell, J. E. T., Singer, B. S., & Jicha, B. R. (2020). Timing of quaternary geomagnetic reversals and excursions in volcanic and sedimentary archives. *Quaternary Science Reviews*, *228*, 106114. <https://doi.org/10.1016/j.quascirev.2019.106114>
- Clark, P. U., Archer, D., Pollard, D., Blum, J. D., Rial, J. A., Brovkin, V., et al. (2006). The middle Pleistocene transition: characteristics, mechanisms, and implications for long-term changes in atmospheric pCO₂. *Quaternary Science Reviews*, *25*(23–24), 3150–3184. <https://doi.org/10.1016/j.quascirev.2006.07.008>
- Clement, B. M. (2004). Dependence of the duration of geomagnetic polarity reversals on site latitude. *Nature*, *428*(6983), 637–640. <https://doi.org/10.1038/nature02459>
- de Boer, B., Lourens, L. J., & van de Wal, R. S. W. (2014). Persistent 400,000-year variability of Antarctic ice volume and the carbon cycle is revealed throughout the Plio-Pleistocene. *Nature Communications*, *5*(1), 2999. <https://doi.org/10.1038/ncomms3999>
- De Vleeschouwer, D., Dunlea, A. G., Gerald, A., Anderson, C. H., Hans, B., de Loach Aaron, et al. (2017). Quantifying K, U, and Th contents of marine sediments using shipboard natural gamma radiation spectra measured on DV JOIDES Resolution. *Geochemistry, Geophysics, Geosystems*, *18*(3), 1053–1064. <https://doi.org/10.1002/2016GC006715>
- Egli, R., & Zhao, X. (2015). Natural remanent magnetization acquisition in bioturbated sediment: General theory and implications for relative paleointensity reconstructions. *Geochemistry, Geophysics, Geosystems*, *16*(4), 995–1016. <https://doi.org/10.1002/2014GC005672>
- Elderfield, H., Ferretti, P., Greaves, M., Crowhurst, S., McCave, I. N., Hodell, D., & Piotrowski, A. M. (2012). Evolution of ocean temperature and ice volume through the mid-Pleistocene climate transition. *Science*, *337*(6095), 704–709. <https://doi.org/10.1126/science.1221294>
- Fisher, R. (1953). Dispersion on a sphere. *Proceedings of the National Academy of Sciences of the United States of America*, *217*(1130), 295–305.
- Ford, H. L., Sosdian, S. M., Rosenthal, Y., & Raymo, M. E. (2016). Gradual and abrupt changes during the mid-Pleistocene transition. *Quaternary Science Reviews*, *148*, 222–233. <https://doi.org/10.1016/j.quascirev.2016.07.005>
- Gohl, K., Wellner, J. S., & Klaus, A. (2019). *Expedition 379 preliminary report: Amundsen Sea West Antarctic ice sheet history*. International Ocean Discovery Program.
- Gradstein, F. M., Ogg, J., Schmitz, M., & Ogg, G. (Eds.), (2012). *The geologic time scale 2012* (1st ed.). Oxford, UK: Elsevier.
- Grant, G. R., Naish, T. R., Dunbar, G. B., Stocchi, P., Kominz, M. A., Kamp, P. J. J., et al. (2019). The amplitude and origin of sea-level variability during the Pliocene epoch. *Nature*, *574*(7777), 237–241. <https://doi.org/10.1038/s41586-019-1619-z>
- Gulick, S. P. S., Jaeger, J. M., Mix, A. C., Asahi, H., Bahlburg, H., Belanger, C. L., et al. (2015). Mid-Pleistocene climate transition drives net mass loss from rapidly uplifting St. Elias Mountains, Alaska. *Proceedings of the National Academy of Sciences of the United States of America*, *112*(49), 15042–15047. <https://doi.org/10.1073/pnas.1512549112>
- Hatfield, R. G., Woods, A., Lehmann, S. B., Weidhaas, N., Chen, C. Y., Kück, J., et al. (2020). Stratigraphic correlation and splice generation for sediments recovered from a large-lake drilling project: an example from Lake Junin, Peru. *Journal of Paleolimnology*, *63*(1), 83–100. <https://doi.org/10.1007/s10933-019-00098-w>
- Hays, J. D., Imbrie, J., & Shackleton, N. J. (1976). Variations in the Earth's orbit: Pacemaker of the ice ages. *Science*, *194*(4270), 1121–1132.
- Hodell, D. A., & Channell, J. E. T. (2016). Mode transitions in Northern Hemisphere glaciation: Co-evolution of millennial and orbital variability in Quaternary climate. *Climate of the Past*, *12*(9), 1805.
- Hodell, D. A., Channell, J. E. T., Curtis, J. H., Romero, O. E., & Röhl, U. (2008). Onset of “Hudson Strait” Heinrich events in the eastern North Atlantic at the end of the middle Pleistocene transition (~640 ka)? *Paleoceanography*, *23*(4), 1–16. <https://doi.org/10.1029/2008PA001591>
- Hong, C.-S., Lee, M.-Y., Pälike, H., Wei, K.-Y., Liang, W.-T., Iizuka, Y., & Torii, M. (2002). Astronomically calibrated ages for geomagnetic reversals within the Matuyama chron. *Earth, Planets and Space*, *54*, 679–690.
- Hospers, J. (1954). Rock magnetism and polar wandering. *Nature*, *173*(4416), 1183–1184. <https://doi.org/10.1038/1731183a0>
- Husson, D., Thibault, N., Galbrun, B., Gardin, S., Minoletti, F., Sageman, B., & Huret, E. (2014). Lower Maastrichtian cyclostratigraphy of the Bidart section (Basque Country, SW France): A remarkable record of precessional forcing. *Palaeogeography, Palaeoclimatology, Palaeoecology*, *395*, 176–197. <https://doi.org/10.1016/j.palaeo.2013.12.008>
- Huybers, P. (2006). Early Pleistocene glacial cycles and the integrated summer insolation forcing. *Science*, *313*(5786), 508–511.
- Huybers, P. (2007). Glacial variability over the last two million years: an extended depth-derived agemodel, continuous obliquity pacing, and the Pleistocene progression. *Quaternary Science Reviews*, *26*(1–2), 37–55.
- Imbrie, J., Hays, J. D., Martinson, D. G., McIntyre, A., Mix, A. C., Morley, J. J., et al. (1984). The orbital theory of Pleistocene climate: support from a revised chronology of the marine d18O record. In A. Berger (Ed.), *Milankovitch and climate, Part 1* (pp. 269–305). New York, NY: Springer.
- Imbrie, J., & Imbrie, J. Z. (1980). Modeling the climatic response to orbital variations. *Science*, *207*(4434), 943–953. <https://doi.org/10.1126/science.207.4434.943>
- Irving, E., & Major, A. (1964). Post-depositional detrital remanent magnetization in a synthetic sediment. *Sedimentology*, *3*(2), 135–143. <https://doi.org/10.1111/j.1365-3091.1964.tb00638.x>
- Jansen, E., Fronval, T., Rack, F., & Channell, J. E. T. (2000). Pliocene-Pleistocene ice rafting history and cyclicity in the Nordic Seas during the last 3.5 Myr. *Paleoceanography*, *15*(6), 709–721. <https://doi.org/10.1029/1999PA000435>
- Laskar, J., Joutel, F., & Boudin, F. (1993). Orbital, precessional, and insolation quantities for the Earth from –20 Myr to +10 Myr. *Astronomy and Astrophysics*, *270*(1–2), 522–533.
- Laskar, J., Robutel, P., Joutel, F., Gastineau, M., Correia, A. C. M., & Levrard, B. (2004). A long-term numerical solution for the insolation quantities of the Earth. *Astronomy & Astrophysics*, *428*(1), 261–285. <https://doi.org/10.1051/0004-6361:20041335>

- Liautaud, P. R., Hodell, D. A., & Huybers, P. J. (2020). Detection of significant climatic precession variability in early Pleistocene glacial cycles. *Earth and Planetary Science Letters*, 536, 116137. <https://doi.org/10.1016/j.epsl.2020.116137>
- Lisiecki, L. E., & Herbert, T. D. (2007). Automated composite depth scale construction and estimates of sediment core extension. *Paleoceanography*, 22(4), 1–12. <https://doi.org/10.1029/2006PA001401>
- Lisiecki, L. E., & Raymo, M. E. (2005). A Pliocene-Pleistocene stack of 57 globally distributed benthic $\delta^{18}\text{O}$ records. *Paleoceanography*, 20(1), PA1003. <https://doi.org/10.1029/2004PA001071>
- Lisiecki, L. E., & Raymo, M. E. (2007). Plio-Pleistocene climate evolution: trends and transitions in glacial cycle dynamics. *Quaternary Science Reviews*, 26(1–2), 56–69. <https://doi.org/10.1016/j.quascirev.2006.09.005>
- Lisiecki, L. E., & Stern, J. V. (2016). Regional and global benthic $\delta^{18}\text{O}$ stacks for the last glacial cycle. *Paleoceanography and Paleoclimatology*, 31(10), 1368–1394. <https://doi.org/10.1002/2016PA003002>
- Lougheed, B., & Obrochta, S. (2019). A rapid, deterministic age-depth modeling routine for geological sequences with inherent depth uncertainty. *Paleoceanography and Paleoclimatology*, 34(1), 122–133. <https://doi.org/10.1029/2018PA003457>
- Lourens, L. J., Antonarakou, A., Hilgen, F. J., Van Hoof, A. A. M., Vergnaud-Grazzini, C., & Zachariasse, W. J. (1996). Evaluation of the Plio-Pleistocene astronomical timescale. *Paleoceanography and Paleoclimatology*, 11(4), 391–413.
- Lourens, L. J., & Hilgen, F. J. (1997). Long-periodic variations in the earth's obliquity and their relation to third-order eustatic cycles and late Neogene glaciations. *Quaternary International*, 40, 43–52. [https://doi.org/10.1016/S1040-6182\(96\)00060-2](https://doi.org/10.1016/S1040-6182(96)00060-2)
- Maldonado, A., Barnolas, A., Bohoyo, F., Galindo-Zaldívar, J., Hernández-Molina, J., Lobo, F., et al. (2003). Contourite deposits in the central Scotia Sea: the importance of the Antarctic Circumpolar Current and the Weddell Gyre flows. *Palaeogeography, Palaeoclimatology, Palaeoecology*, 198(1–2), 187–221.
- McElhinny, M. W. (2007). Geocentric axial dipole hypothesis. In D. Gubbins, & E. Herrero-Bervera (Eds.), *Encyclopedia of geomagnetism and paleomagnetism* (pp. 281–287). The Netherlands: Springer. https://doi.org/10.1007/978-1-4020-4423-6_107
- Meredith, M. P., Garabato, A. C. N., Gordon, A. L., & Johnson, G. C. (2008). Evolution of the deep and bottom waters of the Scotia Sea, Southern Ocean, during 1995–2005. *Journal of Climate*, 21(13), 3327–3343. <https://doi.org/10.1175/2007JCL12238.1>
- Mix, A. C. (2020). On quantifying stratigraphic, chronologic, and paleo flux uncertainties in paleoceanography. *Oceanography*, 33(2), 29–31. <https://doi.org/10.5670/oceanog.2020.223>
- Morée, A. L., Sun, T., Bretones, A., Straume, E. O., Nisancioglu, K., & Gebbie, G. (2021). Cancellation of the precessional cycle in $\delta^{18}\text{O}$ records during the Early Pleistocene. *Geophysical Research Letters*, 48. <https://doi.org/10.1029/2020gl090035>
- Naish, T., Powell, R., Levy, R., Wilson, G., Scherer, R., Talarico, F., et al. (2009). Obliquity-paced Pliocene West Antarctic ice sheet oscillations. *Nature*, 458(7236), 322–328. <https://doi.org/10.1038/nature07867>
- Opdyke, N. D., Glass, B., Hays, J. D., & Foster, J. (1966). Paleomagnetic study of Antarctic deep-sea cores. *Science*, 154(3747), 349–357.
- Pälike, H., Norris, R. D., Herrle, J. O., Wilson, P. A., Coxall, H. K., Lear, C. H., et al. (2006). The heartbeat of the oligocene climate system. *Science*, 314(5807), 1894–1898. <https://doi.org/10.1126/science.1133822>
- Patterson, M. O., McKay, R., Naish, T., Escutia, C., Jimenez-Espejo, F. J., Raymo, M. E., et al. (2014). Orbital forcing of the East Antarctic ice sheet during the Pliocene and Early Pleistocene. *Nature Geoscience*, 7(11), 841–847. <https://doi.org/10.1038/ngeo2273>
- Pérez, L. F., Maldonado, A., Hernández-Molina, F. J., Lodolo, E., Bohoyo, F., & Galindo-Zaldívar, J. (2017). Tectonic and oceanographic control of sedimentary patterns in a small oceanic basin: Dove Basin (Scotia Sea, Antarctica). *Basin Research*, 29, 255–276.
- Pérez, L. F., Martos, Y. M., García, M., Weber, M. E., Raymo, M. E., Williams, T., et al. (2021). Miocene to present oceanographic variability in the Scotia Sea and Antarctic ice sheets dynamics: Insight from revised seismic-stratigraphy following IODP Expedition 382. *Earth and Planetary Science Letters*, 553, 116657. <https://doi.org/10.1016/j.epsl.2020.116657>
- Pisias, N. G., & Moore, T. C., Jr (1981). The evolution of Pleistocene climate: a time series approach. *Earth and Planetary Science Letters*, 52(2), 450–458.
- Pollard, D., & DeConto, R. M. (2009). Modeling West Antarctic ice sheet growth and collapse through the past five million years. *Nature*, 458(7236), 329–332. <https://doi.org/10.1038/nature07809>
- Raymo, M. E., & Huybers, P. (2008). Unlocking the mysteries of the ice ages. *Nature*, 451(7176), 284–285. <https://doi.org/10.1038/nature06589>
- Raymo, M. E., Lisiecki, L. E., & Nisancioglu, K. H. (2006). Plio-Pleistocene ice volume, Antarctic climate, and the global $\delta^{18}\text{O}$ record. *Science*, 313(5786), 492–495.
- Raymo, M. E., & Nisancioglu, K. H. (2003). The 41 kyr world: Milankovitch's other unsolved mystery. *Paleoceanography and Paleoclimatology*, 18(1), 1–6. <https://doi.org/10.1029/2002PA000791>
- Raymo, M. E., Ruddiman, W. F., Backman, J., Clement, B. M., & Martinson, D. G. (1989). Late Pliocene variation in northern hemisphere ice sheets and North Atlantic deep water circulation. *Paleoceanography and Paleoclimatology*, 4(4), 413–446. <https://doi.org/10.1029/PA004i004p00413>
- Richter, C., Acton, G., Endris, C., & Radsted, M. (2007). *Handbook for shipboard paleomagnetists (ODP Tech. Note. 34)*. International Ocean Discovery Program. Retrieved from http://www-odp.tamu.edu/Publications/tnotes/tn34/tn34_.htm
- Rohling, E. J., Foster, G. L., Grant, K. M., Marino, G., Roberts, A. P., Tamisiea, M. E., & Williams, F. (2014). Sea-level and deep-sea-temperature variability over the past 5.3 million years. *Nature*, 508(7497), 477–482. <https://doi.org/10.1038/nature13230>
- Ruddiman, W. F., Cameron, D., & Clement, B. (1987). Sediment disturbance and correlation of offset holes drilled with the hydraulic piston corer: Leg 94. In Susan, O., Initial reports of the deep sea drilling project (Vol. 94). <https://doi.org/10.2973/dsdp.proc.94.1987>
- Ruddiman, W. F., Kidd, R. B., Baldauf, J., Clement, B., Dolan, J., Eggers, M., et al. (1987). Initial reports of the deep sea drilling project (Vol. 94). Washington DC: U.S. Government Printing Office. <https://doi.org/10.2973/dsdp.proc.94.1987>
- Ruddiman, W. F., Raymo, M. E., Martinson, D. G., Clement, B. M., & Backman, J. (1989). Pleistocene evolution: Northern hemisphere ice sheets and North Atlantic Ocean. *Paleoceanography and Paleoclimatology*, 4(4), 353–412. <https://doi.org/10.1029/PA004i004p00353>
- Ruddiman, W. F., Raymo, M., & McIntyre, A. (1986). Matuyama 41,000-year cycles: North Atlantic Ocean and northern hemisphere ice sheets. *Earth and Planetary Science Letters*, 80(1), 117–129. [https://doi.org/10.1016/0012-821X\(86\)90024-5](https://doi.org/10.1016/0012-821X(86)90024-5)
- Ryan, W. B. F., Carbotte, S. M., Coplan, J. O., O'Hara, S., Melkonian, A., Arko, R., et al. (2009). Global Multi-Resolution Topography synthesis. *Geochemistry, Geophysics, Geosystems*, 10, Q03014. <https://doi.org/10.1029/2008GC002332>
- Scherer, R. P., Bohaty, S. M., Dunbar, R. B., Esper, O., Flores, J.-A., Gersonde, R., et al. (2008). Antarctic records of precession-paced insolation-driven warming during early Pleistocene Marine Isotope Stage 31. *Geophysical Research Letters*, 35, L03505. <https://doi.org/10.1029/2007GL032254>
- Shackleton, N. J. (1967). Oxygen isotope analyses and Pleistocene temperatures re-assessed. *Nature*, 215(5096), 15–17.
- Shackleton, N. J., Backman, J., Zimmerman, H. t, Kent, D. V., Hall, M. A., Roberts, D. G., et al. (1984). Oxygen isotope calibration of the onset of ice-rafting and history of glaciation in the North Atlantic region. *Nature*, 307(5952), 620–623.

- Shackleton, N. J., Berger, A., & Peltier, W. R. (1990). An alternative astronomical calibration of the lower Pleistocene timescale based on ODP Site 677. *Earth and Environmental Science Transactions of the Royal Society of Edinburgh*, 81(4), 251–261.
- Shackleton, N. J., Crowhurst, S., Hageberg, T., Pisias, N. G., & Schneider, D. A. (1995). A new late Neogene time scale: application to Leg 138 sites. *Proceedings of the Ocean Drilling Program*, 138, 73–101.
- Shackleton, N. J., & Opdyke, N. D. (1973). Oxygen isotope and paleomagnetic stratigraphy of Equatorial Pacific core V28-238: Oxygen isotope temperatures and ice volumes on a 105 year and 106 year scale. *Quaternary Research*, 3(1), 39–55. [https://doi.org/10.1016/0033-5894\(73\)90052-5](https://doi.org/10.1016/0033-5894(73)90052-5)
- Shakun, J. D., Raymo, M. E., & Lea, D. W. (2016). An early Pleistocene Mg/Ca- $\delta^{18}\text{O}$ record from the Gulf of Mexico: Evaluating ice sheet size and pacing in the 41-kyr world. *Paleoceanography and Paleoclimatology*, 31(7), 1011–1027. <https://doi.org/10.1002/2016PA002956>
- Simon, Q., Bourlès, D. L., Thouveny, N., Horng, C.-S., Valet, J.-P., Bassinot, F., & Choy, S. (2018). Cosmogenic signature of geomagnetic reversals and excursions from the Réunion event to the Matuyama–Brunhes transition (0.7–2.14 Ma interval). *Earth and Planetary Science Letters*, 482, 510–524. <https://doi.org/10.1016/j.epsl.2017.11.021>
- Sosdian, S., & Rosenthal, Y. (2009). Deep-sea temperature and ice volume changes across the Pliocene–Pleistocene climate transitions. *Science*, 325(5938), 306–310. <https://doi.org/10.1126/science.1169938>
- Sprenk, D., Weber, M. E., Kuhn, G., Rosén, P., Frank, M., Molina-Kescher, M., et al. (2013). Southern Ocean bioproductivity during the last glacial cycle—New detection method and decadal-scale insight from the Scotia Sea. *Geological Society, London, Special Publications*, 381(1), 245–261. <https://doi.org/10.1144/SP381.17>
- Stephenson, A. (1993). Three-axis static alternating field demagnetization of rocks and the identification of natural remanent magnetization, gyroremanent magnetization, and anisotropy. *Journal of Geophysical Research*, 98(B1), 373–381. <https://doi.org/10.1029/92JB01849>
- Stoner, J. S., Channell, J. E. T., Mazaud, A., Strano, S. E., & Xuan, C. (2013). The influence of high-latitude flux lobes on the Holocene paleomagnetic record of IODP Site U1305 and the northern North Atlantic. *Geochemistry, Geophysics, Geosystems*, 14(10), 4623–4646. <https://doi.org/10.1002/ggge.20272>
- Tauxe, L., Herbert, T., Shackleton, N. J., & Kok, Y. S. (1996). Astronomical calibration of the Matuyama–Brunhes boundary: Consequences for magnetic remanence acquisition in marine carbonates and the Asian loess sequences. *Earth and Planetary Science Letters*, 140(1–4), 133–146.
- Thébaud, E., Finlay, C. C., Beggan, C. D., Alken, P., Aubert, J., Barrois, O., et al. (2015). International Geomagnetic Reference Field: The 12th generation. *Earth, Planets and Space*, 67, 79. <https://doi.org/10.1186/s40623-015-0228-9>
- Timmermann, A., Friedrich, T., Timm, O. E., Chikamoto, M. O., Abe-Ouchi, A., & Ganopolski, A. (2014). Modeling obliquity and CO₂ effects on Southern Hemisphere climate during the past 408 ka*. *Journal of Climate*, 27(5), 1863–1875. <https://doi.org/10.1175/JCLI-D-13-00311.1>
- Valet, J.-P., Bassinot, F., Simon, Q., Savranskaia, T., Thouveny, N., Bourlès, D. L., & Villedieu, A. (2019). Constraining the age of the last geomagnetic reversal from geochemical and magnetic analyses of Atlantic, Indian, and Pacific Ocean sediments. *Earth and Planetary Science Letters*, 506, 323–331. <https://doi.org/10.1016/j.epsl.2018.11.012>
- Walczak, M. H., Mix, A. C., Willse, T., Slagle, A., Stoner, J. S., Jaeger, J., et al. (2015). Correction of non-intrusive drill core physical properties data for variability in recovered sediment volume. *Geophysical Journal International*, 202(2), 1317–1323. <https://doi.org/10.1093/gji/ggv204>
- Weber, M. E., Clark, P. U., Kuhn, G., Timmermann, A., Sprenk, D., Gladstone, R., et al. (2014). Millennial-scale variability in Antarctic ice-sheet discharge during the last deglaciation. *Nature*, 510(7503), 134–138. <https://doi.org/10.1038/nature13397>
- Weber, M. E., Kuhn, G., Sprenk, D., Rolf, C., Ohlwein, C., & Ricken, W. (2012). Dust transport from Patagonia to Antarctica—A new stratigraphic approach from the Scotia Sea and its implications for the last glacial cycle. *Quaternary Science Reviews*, 36, 177–188. <https://doi.org/10.1016/j.quascirev.2012.01.016>
- Weber, M. E., Niessen, F., Kuhn, G., & Wiedicke, M. (1997). Calibration and application of marine sedimentary physical properties using a multi-sensor core logger. *Marine Geology*, 136(3), 151–172.
- Weber, M. E., Raymo, M. E., Peck, V. L., & Williams, T., & The Expedition 382 Scientists. (2019). *International Ocean Discovery Program Expedition 382 preliminary report: Iceberg Alley and SubAntarctic Ice and Ocean Dynamics*. International Ocean Discovery Program Preliminary Report.
- Weber, M. E., & Reilly, B. T. (2018). Hemipelagic and turbiditic deposits constrain lower Bengal Fan depositional history through Pleistocene climate, monsoon, and sea level transitions. *Quaternary Science Reviews*, 199, 159–173. <https://doi.org/10.1016/j.quascirev.2018.09.027>
- Zachariasse, W. J., Gudjonsson, L., Hilgen, F. J., Langereis, C. G., Lourens, L. J., Verhallen, P., & Zijderveld, J. D. A. (1990). Late Gauss to early Matuyama invasions of Neogloboquadrina Atlantica in the Mediterranean and associated record of climatic change. *Paleoceanography and Paleoclimatology*, 5(2), 239–252.
- Zachariasse, W. J., Zijderveld, J. D. A., Langereis, C. G., Hilgen, F. J., & Verhallen, P. (1989). Early late Pliocene biochronology and surface water temperature variations in the Mediterranean. *Marine Micropaleontology*, 14(4), 339–355.
- Zijderveld, J. D. A. (1967). AC demagnetization of rocks: analysis of results. *Methods in Paleomagnetism*, 1, 254–286.